Geophysical Journal International

Geophys. J. Int. (2016) **206,** 757–773
Advance Access publication 2016 April 28
GJI Seismology

doi: 10.1093/gji/ggw172

Evidence for non-self-similarity of microearthquakes recorded at a Taiwan borehole seismometer array

Yen-Yu Lin,[1,2] Kuo-Fong Ma,[1,2] Hiroo Kanamori,[3] Teh-Ru Alex Song,[4] Nadia Lapusta[3,5] and Victor C. Tsai[3]

[1] *Department of Earth Sciences, National Central University, Taoyuan, Taiwan. E-mail: yylin@earth.sinica.edu.tw*
[2] *Institute of Earth Sciences, Academia Sinica, Taipei, Taiwan*
[3] *Division of Geological and Planetary Sciences, California Institute of Technology, Pasadena, CA, USA*
[4] *Department of Earth Sciences, University College London, London, United Kingdom*
[5] *Division of Engineering and Applied Science, California Institute of Technology, Pasadena, CA, USA*

Accepted 2016 April 25. Received 2016 April 22; in original form 2015 September 4

SUMMARY

We investigate the relationship between seismic moment M_0 and source duration t_w of microearthquakes by using high-quality seismic data recorded with a vertical borehole array installed in central Taiwan. We apply a waveform cross-correlation method to the three-component records and identify several event clusters with high waveform similarity, with event magnitudes ranging from 0.3 to 2.0. Three clusters—Clusters A, B and C—contain 11, 8 and 6 events with similar waveforms, respectively. To determine how M_0 scales with t_w, we remove path effects by using a path-averaged Q. The results indicate a nearly constant t_w for events within each cluster, regardless of M_0, with mean values of t_w being 0.058, 0.056 and 0.034 s for Clusters A, B and C, respectively. Constant t_w, independent of M_0, violates the commonly used scaling relation $t_w \propto M_0^{1/3}$. This constant duration may arise either because all events in a cluster are hosted on the same isolated seismogenic patch, or because the events are driven by external factors of constant duration, such as fluid injections into the fault zone. It may also be related to the earthquake nucleation size.

Key words: Earthquake dynamics; Earthquake source observations; Seismic attenuation.

1 INTRODUCTION

If earthquakes are self-similar, then the source duration t_w (or, equivalently, the corner frequency) should scale with $M_0^{1/3}$, where M_0 is the seismic moment (e.g. Aki 1967). However, several studies have found that some earthquakes have similar source durations regardless of their size. For example, from a study of small earthquakes in Parkfield, California, Harrington & Brodsky (2009) found different seismic moments that correspond to the same minimum source dimension, and Bouchon *et al*. (2011) made a similar observation for repeating earthquakes with stress drop variation in the earthquake sequence preceding the 1999 Izmit earthquake in Turkey. Lengliné *et al*. (2014) discovered that microearthquakes induced by a fluid injection test exhibited a large variability in stress drop, and they suggested that the variations may result from fluid pressure at a localized interface that reduces the normal stress. These observations suggest non-self-similar seismic source behaviour.

If a minimum rupture size is required for an earthquake to nucleate, as suggested, for example, by rate-and-state friction laws (e.g. Rice & Ruina 1983; Rice 1993; Rubin & Ampuero 2005; Lapusta & Liu 2009), the conventional relation $t_w \propto M_0^{1/3}$, which characterises earthquake self-similarity, may break down at a certain magnitude. For example, events could have sizes dictated by the nucleation length but have different stress drops and hence different moments. However, the minimum rupture size of natural earthquakes has not been directly determined.

Although the source scaling relationship $t_w \propto M_0^{1/3}$ has been observed for a wide range of earthquakes (e.g. Allmann & Shearer 2009; Duputel *et al*. 2013), it has also been a subject of debate, especially for small earthquakes (Abercrombie 1995; Ide *et al*. 2004; Stork & Ito 2004; Oye *et al*. 2005; Venkataraman *et al*. 2006; Yamada *et al*. 2007). Conventionally, the source duration of an event is determined from the spectral corner frequency by considering a frequency-dependent (Stork & Ito 2004; Oye *et al*. 2005) or frequency-independent Q-model to remove path effects. It has been suggested that incomplete removal of path effects and an inappropriate instrumental bandwidth affect observed scaling relations (e.g. Ide *et al*. 2003). To reduce the influence of the path effect on source duration estimates, some studies have deconvolved target event records relative to a small event record (Ide *et al*. 2003, 2004; Mori *et al*. 2003; Oye *et al*. 2005; Venkataraman *et al*. 2006; Mayeda & Malagnini 2009; Lin *et al*. 2012). This method is generally called the empirical Green's function (EGF) method.

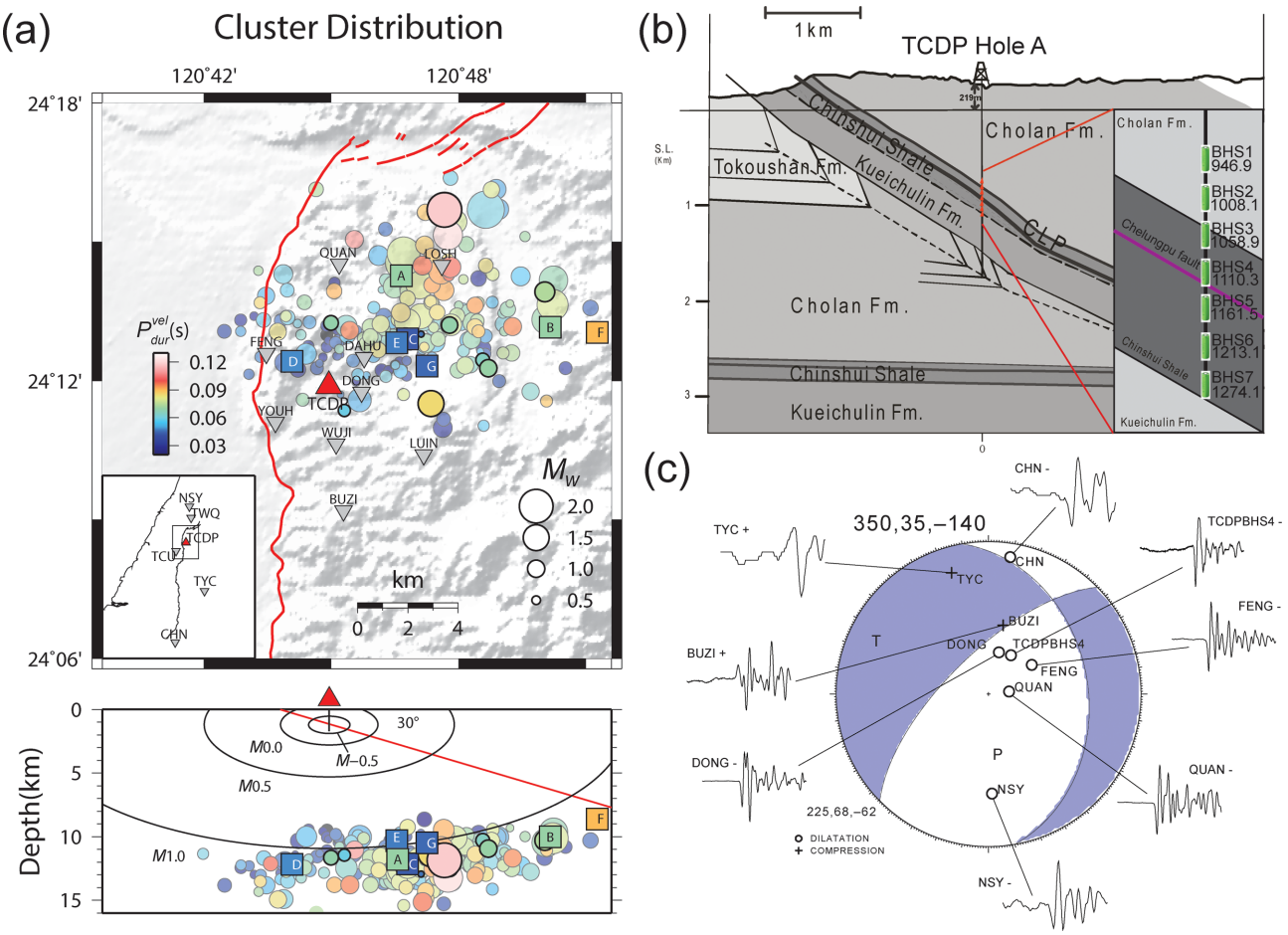

Figure 1. (a) Distribution of the clusters (squares) and background earthquakes (circles). The colour and size of the circles indicate the duration P^{vel}_{dur} and magnitude of the events, respectively. The waveforms of some of the background events are shown in Fig. 4(d). The red triangle and red lines indicate the surface locations of the Taiwan Chelungpu-Fault Drilling Project borehole seismometer array (TCDPBHS) and Chelungpu fault, respectively. The grey inverted triangles show the distribution of the surface seismic stations. Ellipses in the lower figure show the microearthquake detection capability of the TCDPBHS. (b) The layout of the TCDPBHS (modified from Lin *et al*. 2012). The seven stations are located over the depth range from 946 to 1274 m at 50 to 60 m depth intervals (right section, green rectangles). Station no. 4 (BHS4) was installed very close to the Chelungpu main fault (right section, purple line) inside the Chinshui shale. (c) The focal mechanism of an event in Cluster A determined from the *P*-wave first-motion solution obtained using the method of Reasenberg & Oppenheimer (1985). The traces represent *P*-wave waveforms from the stations. The crosses and circles indicate the upward and downward *P*-wave first motion, respectively. The best pairs of nodal planes are 350, 35, −140 and 225, 68, −62, where each set of three values denotes the strike, dip and rake, respectively.

Lin *et al*. (2012) investigated the seismic activity and scaling relationships of microearthquakes recorded with a vertical borehole seismometer array in Taiwan (Fig. 1a). They determined the source parameters, such as the corner frequency and seismic moment, by using a frequency-domain spectral fitting method, Brune's omega-squared source model (Brune 1970) and a frequency-independent *Q*-model. Source dimensions were estimated from corner frequencies. They found that in the magnitude range from M_w 0.0 to 2.0, source dimensions were essentially constant and stress drop increased with magnitude. They also analysed 14 events from several seismic clusters by using the EGF method to remove path effects. The results supported the conclusion obtained using the spectral fitting method. However, some ambiguity in the determined microearthquake scaling relations still remained because of the difficulty in removing path effects completely and the limited frequency bandwidth of the instruments.

In this study, we extend the study of Lin *et al*. (2012) by applying a waveform cross-correlation method to three-component records. (In the study of Lin *et al*. 2012, only the vertical component was used.) The consideration of all three components enables us to use *S*-wave information to define the similarity of waveforms accurately, thus allowing us to include more events in clusters with similar waveforms. In particular, we identify three clusters—Clusters A, B and C—containing 11, 8 and 6 events with similar waveforms, respectively. The consideration of all three components results in a considerably larger database. Moreover, we use several methods to assess the path effects for determining upper and lower bounds on source duration without considering the omega-squared source model whereas Lin *et al*. (2012) used the omega-squared source model as a reference spectrum. Although the omega-squared source model has been established as a useful reference model for small earthquakes, we do not apply it here because we do not want our conclusion to be influenced by the use of a particular source model. We focus on Clusters A, B and C and examine the scaling problem for small earthquakes by considering a set of well-constrained source parameters.

We find that source duration is nearly constant within each cluster, regardless of event magnitude, with mean values of the source

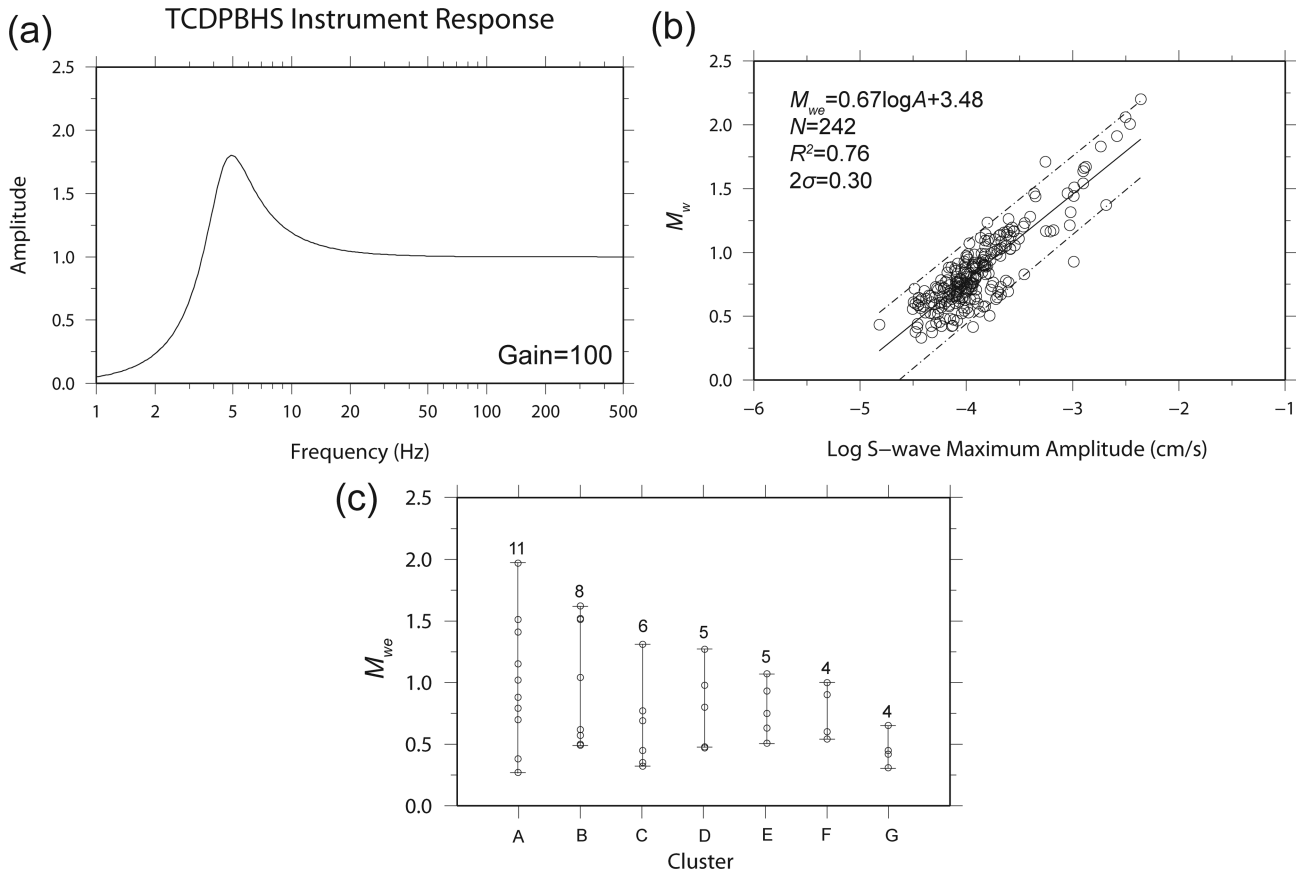

Figure 2. (a) Instrument response of the TCDPBHS. (b) Regression analysis of the maximum *S*-wave amplitude of the horizontal vector sum A (cm s^{-1}) and M_w. The circles show 242 microearthquakes observed by the TCDPBHS (Lin *et al*. 2012). The regression line $M_{we} = 0.67 \log A + 3.48$ is indicated by a solid line. Magnitudes estimated from this empirical relation are called empirical M_w (M_{we}). We ignore the hypocentre distance term in the regression because all microearthquakes occurred at approximately the same hypocentre distances of 10–15 km in the study area. The dotted lines indicate the 95 per cent confidence interval (2σ) of the regression estimates. The variation in M_{we} as estimated from the relation is ±0.3. (c) Distribution of event sizes for Clusters A–G. The circles indicate the magnitudes of the events. The number of events in each cluster is indicated at the top of each bar.

duration being 0.058, 0.056 and 0.034 s for Clusters A, B and C, respectively. The nearly constant durations, independent of M_0, violates the commonly used scaling relation $t_w \propto M_0^{1/3}$.

2 INSTRUMENTATION

The borehole data used in this study were recorded by a seven-level three-component vertical borehole seismic array (TCDPBHS) installed in Hole-A of the Taiwan Chelungpu-Fault Drilling Project (TCDP) in July 2006 (Lin *et al*. 2012; Ma *et al*. 2012; Lin 2014). This array covers a depth range from 946 to 1274 m at intervals of 50–60 m (from the top to the bottom, the seismometers are labelled BHS1 to BHS7; Fig. 1b). Hole-A is a 2 km deep hole that crosses the main fault of the 1999 M_w 7.6 Chi-Chi earthquake (Ma *et al*. 2006) at a depth of 1111 m. The sensors are velocity-type short-period seismometers with a natural frequency of approximately 4.5 Hz, a damping of approximately 29 per cent and a sensitivity of 1.6 V (cm s^{-1})$^{-1}$. Fig. 2(a) shows the average instrument response curve for the 21 sensors at the 7 stations; the curve indicates that the instruments have the capability to record seismic signals higher than 4 Hz. The recording gain is 100. The instrument response was removed from each record, and corrections for the Galperin angle and orientation of the three-component sensors were performed systematically before waveform analysis (Lin *et al*. 2012; Lin 2014). The sampling rate was set at 1000 samples s^{-1} for detecting microearthquakes with high frequency signals up to the end of 2007.

3 DATA

To identify seismic clusters, we employ an improved version of the detection method used by Lin *et al*. (2012). We search for event clusters by cross-correlating over 3278 local microearthquakes that were manually selected by Lin *et al*. (2012); the difference in the arrival time between the *S* wave and the *P* wave is less than or equal to 2.0 s for the microearthquakes. The microearthquakes occurred between November 2006 and December 2007. To compare waveforms of the three-component BHS4 records, we use a 6 s time window from 1 s before to 5 s after the *P*-wave arrival time. Compared with the study of Lin *et al*. (2012), which considered *P*-wave similarity with only vertical component data, we perform a more comprehensive comparison: we compare both *P* and *S* waves with vertical and both horizontal components. For cross-correlation analyses, we use a bandpass filter (10–50 Hz) to capture the dominant frequency band of microearthquakes ($M \leq 2.0$). We group the events into a cluster if the cross-correlation coefficient CC of their three-component waveforms is greater than 0.8. We identify a total of 130 seismic clusters, with each cluster having 2–11 events.

We estimate the magnitudes of these events from maximum *S*-wave vectorial amplitudes (A in cm s^{-1}) by using the empirical

Table 1. Seismic clusters used in this study: results of the EGF and the *Q*-correction methods.

Cluster	Number	Date	Hour	Min	Second	M_{we}	*CC*	Δt_{sp} (s)	P_{dur}^{dis} (s)	EGF		*Q*-correction	
										t_w(s)	Dimension $2r$ (m)	t_w(s)	Dimension $2r$ (m)
A	1	20061126	18	02	173.313	0.38	1.00	1.650	0.068	0.025	103.8	0.054	224.3
	2	20061129	07	37	2223.476	1.51	0.92	1.652	0.071	0.029	120.4	0.062	257.9
	3	20061129	07	37	2240.536	1.02	0.82	1.660	0.072	0.025	103.8	0.063	262.9
	4	20061129	07	37	2254.785	0.70	0.82	1.657	0.068	0.024	99.7	0.059	245.0
	5	20070129	09	34	2051.911	0.79	0.87	1.654	0.071	0.024	99.7	0.064	265.8
	6[a]	20070526	18	48	2892.767	0.27	0.82	1.648	0.074	–	–	0.060	249.2
	7	20070820	13	13	802.829	0.88	0.90	1.648	0.069	0.025	103.8	0.055	228.4
	8	20071018	16	20	1231.643	1.97	0.90	1.647	0.068	0.030	124.6	0.056	230.9
	9	20071018	16	21	1285.838	1.15	0.83	1.641	0.070	0.027	112.1	0.056	232.6
	10	20071020	06	12	751.139	1.41	0.81	1.642	0.072	0.028	116.3	0.060	249.2
	11	20071020	06	33	1996.932	1.51	0.81	1.641	0.068	0.027	112.1	0.054	224.3
B	1	20061124	13	56	3419.909	1.51	1.00	1.800	0.062	–	–	0.058	241.7
	2	20061124	13	59	3566.534	0.50	0.92	1.798	0.065	0.026	108.0	0.056	232.6
	3	20061124	14	01	118.051	1.04	0.93	1.798	0.065	0.025	103.8	0.054	224.3
	4	20061124	14	04	268.517	1.62	0.88	1.805	0.082	0.029	120.4	0.075	311.5
	5	20061124	14	04	275.232	1.52	0.94	1.797	0.069	–	–	0.066	274.1
	6[a]	20061124	19	40	2433.970	0.49	0.85	1.795	0.063	–	–	0.048	199.4
	7	20070101	09	17	1026.288	0.62	0.81	1.811	0.055	–	–	0.047	195.2
	8	20070205	09	00	47.989	0.57	0.85	1.798	0.055	0.025	103.8	0.042	174.4
C	1	20061114	22	38	2286.017	0.77	1.00	1.600	0.039	0.021	87.2	0.033	137.1
	2	20061114	23	14	883.510	0.69	0.95	1.602	0.040	0.024	99.7	0.034	141.2
	3	20061114	23	19	1143.311	1.32	0.94	1.604	0.049	0.025	103.8	0.037	153.7
	4[a]	20061115	00	00	11.242	0.35	0.92	1.598	0.038	–	–	0.032	132.9
	5	20061115	00	17	1042.864	0.45	0.93	1.597	0.038	0.021	87.2	0.032	132.9
	6	20070723	05	59	3560.207	0.94	0.84	1.606	0.051	–	–	0.039	160.3

[a]The smallest event that is used as an empirical Green's function in EGF analysis.

relationship $M_{we} = 0.67 \log A + 3.48$ (Fig. 2b). This relationship was obtained using the 242 located events of the 3278 events identified by Lin *et al*. (2012), where the empirical moment magnitude M_{we} was estimated using spectral analysis and the *S*-wave amplitudes of the 242 located events (Lin *et al*. 2012). The two-sigma variation of M_{we} is approximately ± 0.3.

Among the clusters, seven clusters comprise more than four events (Fig. 2c), and three of them contain events with a magnitude range greater than 1. We label these three clusters A, B and C. The other clusters are labelled D to G. We focus on Clusters A, B and C because they have a large magnitude range of 0.27–1.97, 0.49–1.62 and 0.35–1.32, respectively (Table 1, Fig. 2c).

To locate these clusters, we stack records of the events in each cluster to improve the signal-to-noise (S/N) ratio and then use the *P*-wave polarization angles determined from particle motions and the difference in the arrival time between the *S* wave and the *P* wave. This method was also used to locate microearthquakes using records of the vertical borehole array (Oye & Roth 2003; Lin *et al*. 2012). We assume a laterally homogeneous velocity structure estimated from a 3D velocity model for this area of Taiwan (Kim *et al*. 2005). Since the ray paths to the borehole stations avoid very low velocity shallow structures, we do not expect large velocity variations over the study area, which extends over a few kilometres (Lin *et al*. 2012). Fig. 1(a) shows the distribution of Clusters A to G together with the 242 microearthquakes identified by Lin *et al*. (2012). These event clusters have similar locations to the background seismicity in the depth range of approximately 10–15 km and they are within the deformation zone of a fold-and-thrust system along the decollement (Lin *et al*. 2012).

Focal mechanisms of these event clusters are difficult to determine because of the lack of useful recordings from surface stations. Only one event in Cluster A, with M_{we} 1.51, was well recorded at surface stations (Fig. 1a). Fig. 1(c) shows the first-motion focal mechanism determined using the method described by Reasenberg & Oppenheimer (1985). The focal mechanism has two nodal planes with a strike of 350/225, a dip of 35/68 and a rake of −140/−62; the slip vector suggests oblique motion.

4 SIMILAR *P*-WAVE DURATIONS OF EVENTS IN EACH CLUSTER

We can visually observe that the *P*-wave duration within each event cluster is essentially constant. Fig. 3 shows waveform comparisons between the smallest ($M_{we} = 0.27$) and the largest ($M_{we} = 1.97$) events in Cluster A at stations BHS1 and BHS4. Both *P* and *S* waves show high similarity at both stations, regardless of the event magnitude. We use the original records after instrument and orientation corrections, and a notch filter is applied over the frequency band 58–62 Hz to remove strong electronic noise. Fig. A1 shows examples of the *P*-wave recordings of events in Clusters A, B and C over the stations BHS1–BHS7. Since the records at BHS4 are of higher quality (Lin *et al*. 2012) than those at other borehole stations, we use the waveforms at BHS4 in the following analysis. We focus on *P*-wave duration because the waveforms of *P* waves are simpler than those of *S* waves.

The vertical velocity records at BHS4 show distinct constant P durations in Clusters A, B and C (Figs 4a–c). We measure *P*-wave duration (P_{dur}^{vel}) by identifying zero crossings of the first cycle of the P phase, as illustrated in Fig. 4(a). The parameter P_{dur}^{vel} of Clusters A, B and C is 0.086, 0.081 and 0.053 s, respectively, and the dominant frequency of the *P* waves is approximately 10–20 Hz. Fig. 4(e)

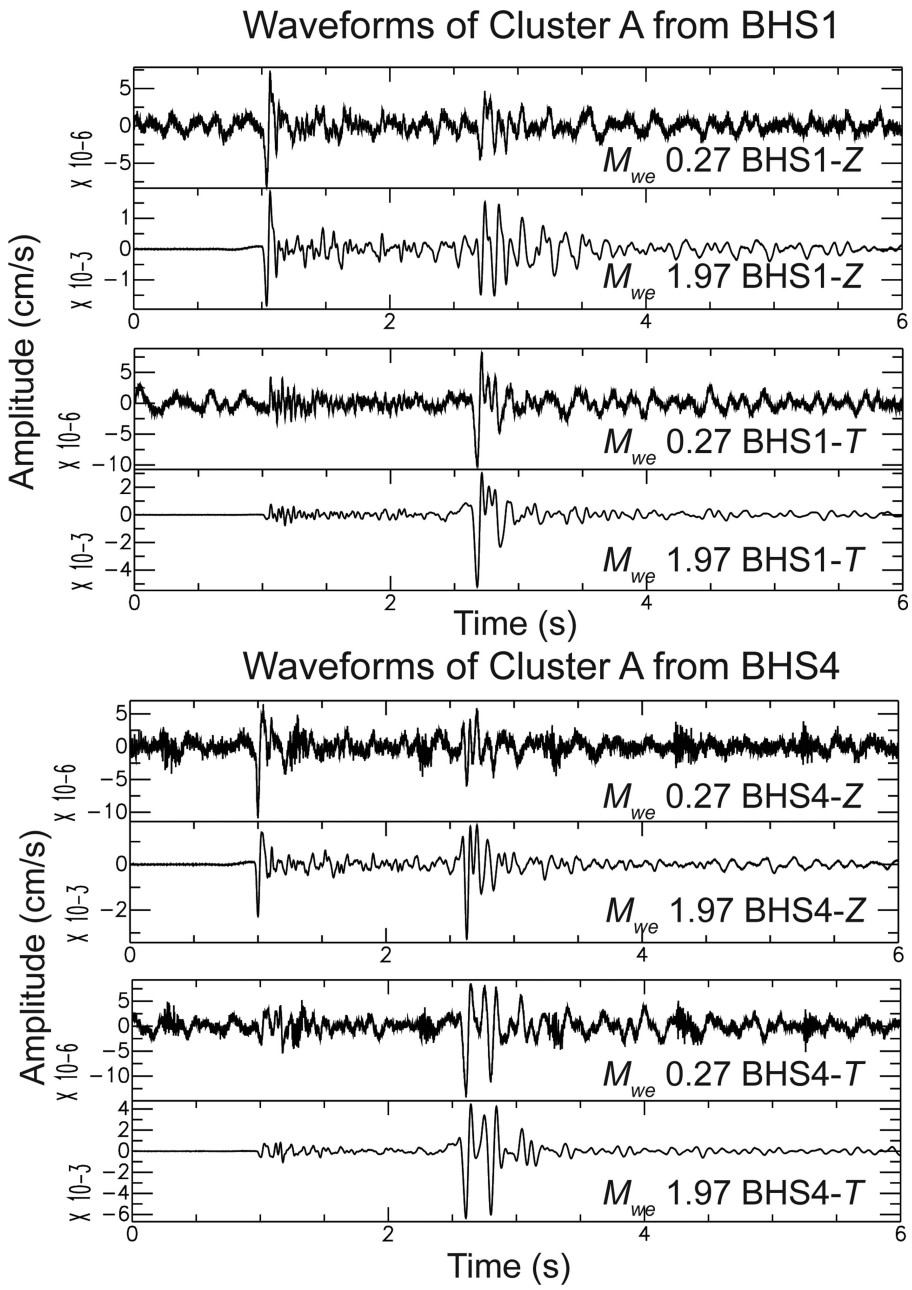

Figure 3. Comparison of the *Z*- and *T*-component waveforms for the smallest (M_{we} 0.27) and largest (M_{we} 1.97) events in Cluster A. The waveforms recorded at BHS1 (upper section) and BHS4 (lower section) are shown; the *P*-wave and *S*-wave observations are reflected in the vertical (*Z*) and transverse (*T*) components, respectively. The smallest event shows higher-frequency content, but the *P*-wave source duration is very similar to that of the largest event. *S* waves for the smaller and larger events are almost identical.

shows the superposition of event waveforms from Clusters A, B and C after amplitude normalization. The superposed waveforms exhibit a consistent initial downward pulse for all events in each cluster, regardless of event magnitude. The constant P_{dur}^{vel} observed in these event clusters is in striking contrast with the variable P_{dur}^{vel} for other events in a similar magnitude range, shown in Fig. 4(d). Fig. 5 compares P_{dur}^{vel} of Clusters A, B and C with that of other microearthquakes with similar magnitudes. The constant P_{dur}^{vel} in Clusters A, B and C is evident.

We determine the difference in the arrival time between the *S* wave and the *P* wave (Δt_{sp}) for events in each cluster by comparing the waveforms of *P* waves in the *Z* component and those of *S* waves in the *N* component. The first event in each cluster is used as a template. We window a 0.4 s record containing *P* and *S* waves from the original seismograms, and determine the *P* and *S* arrival times by cross-correlating the windowed records of the template event with those of other events. With *P* and *S* arrival times thus determined, we compute Δt_{sp}.

In general, difference in Δt_{sp} between the events within a cluster is less than 0.02 s, indicating that the maximum distance between events in a cluster is approximately 160 m. In a medium in which the *P*-wave speed is 5700 m s^{-1}, the wavelength of a *P* wave with a dominant frequency of 10–20 Hz is 285–570 m. Thus, the difference in distance is smaller than the wavelength of the *P* wave, and therefore, we consider the events within a cluster to be from approximately the same location and to have similar path effects.

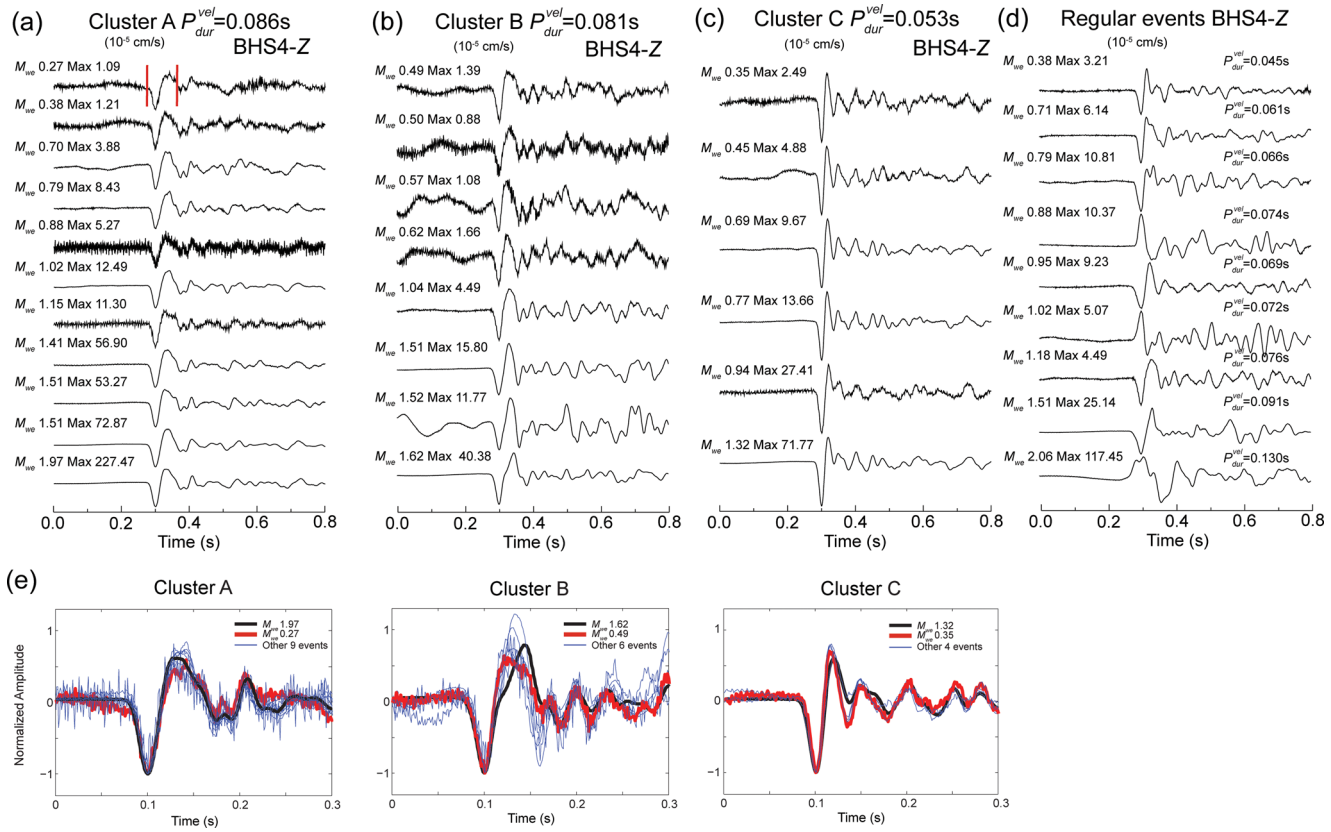

Figure 4. *Z*-component *P*-wave velocity seismograms recorded at BHS4 for (a) Cluster A, (b) Cluster B and (c) Cluster C. Red bars on the first trace in (a) indicate the *P*-wave duration ($P_{\rm dur}^{\rm vel}$) of the event. The maximum amplitude and magnitude $M_{\rm we}$ are mentioned above each trace. (d) Seismograms of regular events. (e) Comparison of the normalized *P* waves for Clusters A (left), B (middle) and C (right), respectively, in a smaller time window (0.3 s). The black and red lines show the records for the largest and smallest events, respectively. The thinner blue lines show seismograms of the other events in each cluster.

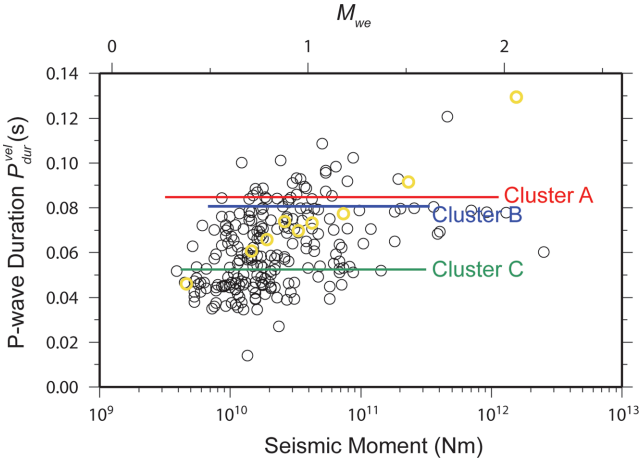

Figure 5. *P*-wave duration ($P_{\rm dur}^{\rm vel}$) versus seismic moment for regular events (black circles) and for events in Clusters A, B and C. The circles show 242 observations (Lin *et al*. 2012). The red, blue and green horizontal lines indicate $P_{\rm dur}^{\rm vel}$ of Clusters A, B and C, respectively, and the yellow circles refer to the regular events shown in Fig. 4(d).

5 SOURCE DURATION ESTIMATES

As shown in Fig. 4, the pulse width of the observed *P* wave is essentially constant regardless of event magnitude. However, this does not necessarily mean that the width of the source pulse is constant. To investigate this question, we first consider the following two end-member models. (1) In the first end-member model, we assume that the observed waveform represents the source-time function (STF). This model can be used to obtain the longest estimate of the STF. (2) In the second end-member model, we assume that the STF of the smallest event is a delta function $\delta(t)$ and that the observed waveform is due to path effects. This model has the potential to yield the shortest estimate of the STF, at least within the signal resolution. Then, we obtain the most plausible durations by correcting the waveforms for attenuation determined for the region in prior studies. We illustrate our analysis for the events in Cluster A. The same analysis is performed for the events in the other clusters.

For the first end-member model, we assume that the path effect is small and that the observed waveforms represent the STFs. The waveforms shown in Fig. 4 are velocity waveforms. Since the source waveform is the moment-rate function (as we shall show later), which corresponds to the displacement waveform, we convert the velocity waveforms in Fig. 4 to displacement waveforms and define their pulse width as follows.

First, we integrate the velocity waveforms in Fig. 4 and apply a zero-phase bandpass filter with a bandwidth of 5–50 Hz. Fig. 6 shows an example of an estimated STF, which typically has a triangular shape. The peak amplitude is denoted by PA, and the two minima on either side of the PA are called the left bottom amplitude (LBA) and right bottom amplitude (RBA). We define the minimum amplitude of the STF as the average of the LBA and RBA. The full amplitude of the STF can be defined as the difference between the PA and the minimum amplitude. The half-amplitude points are shown by dots. The source pulse width t_w is twice the time interval

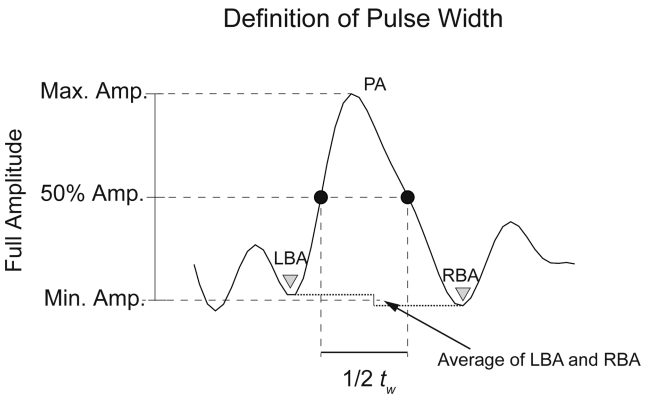

Figure 6. Definition of the displacement source pulse width. The pulse width of the displacement record is defined as t_w. For more details, see the text.

between the two dots. Results for this first end-member are shown in Fig. 7. The *P*-wave pulse width $P_{\rm dur}^{\rm dis}$ thus defined is essentially constant for all the records in each cluster and represents t_w, and is 0.070, 0.065 and 0.043 s for Clusters A, B and C, respectively.

Using the second end-member model, we deconvolve the observed waveforms with that of the smallest event. This method is generally referred to as the EGF method. As shown later, the S/N ratio of the spectra of these events deteriorates at very high frequencies, greater than 50 Hz. Therefore, we filter the deconvolved records using a bandpass filter with a pass band of 5–50 Hz. Fig. 8(a) shows the filtered deconvolved signals for Cluster A. We define the pulse width using the method illustrated in Fig. 6. The top trace labelled 'impulse' is the filtered delta function, which is assumed as the STF for the smallest event. With our definition of the pulse width (illustrated in Fig. 6), the width of this pulse is 0.020 s. The deconvolved source pulses for larger events are slightly broader, and they have a width ranging from 0.024 to 0.030 s for the $M_{\rm we}$ range from 0.38 to 1.97 (Fig. 8 and Table 1). In practice, the resolution may be reduced because of the bandpass filtering (5–50 Hz) of the deconvolved signal, as illustrated in Appendix B for a triangular STF.

The results of the EGF method are consistent with our hypothesis of the near-constant duration of the STFs for the events of different magnitude in each cluster. By assuming that the smallest event is an impulse, or has the duration of 0.020 s when filtered between 5 and 50 Hz, we get similar durations for the other events in the cluster of 0.024–0.030 s. These durations are almost constant in contrast to the behaviour expected of the commonly assumed scaling of $t_w \propto M_0^{1/3}$, as discussed further in the next section.

Given the similarity of the time-domain signals, the broadening of the source pulse widths with respect to the smallest event is somewhat unexpected, but as shown later, the spectral fall-off of larger events is steeper than that of the smallest event over the frequency band 20–50 Hz. This difference in the high-frequency spectral fall-off causes the broadening of the source pulse.

The source pulse widths estimated with the two end-member models bound the real source pulse width. Note that the resolution of deconvolution is naturally limited by the S/N ratio and the pass band of the filter. Although the spectral amplitude of the smallest event appears to be higher than the noise spectral amplitude at frequencies lower than 50 Hz, as shown in Fig. 9, we cannot completely rule out that the spectrum of the smallest event is influenced by noise at lower frequencies and, consequently, that the pulse widths of the

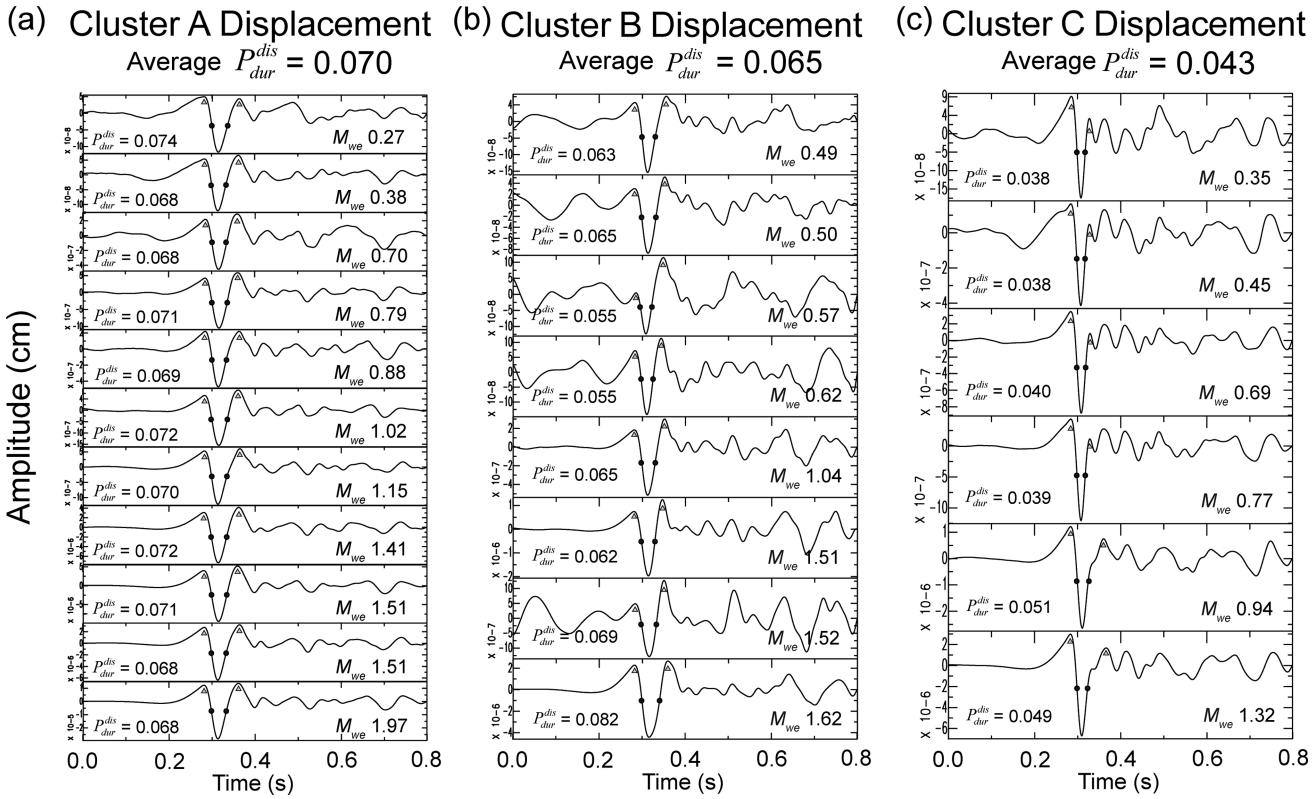

Figure 7. Waveforms (0.8 s resolution) of the *Z*-component (*P* wave) displacement seismograms recorded at BHS4 for (a) Cluster A, (b) Cluster B and (c) Cluster C. The zero-phase bandpass filter with a passband of 5–50 Hz is applied. The black dots indicate half of the *P*-wave duration ($P_{\rm dur}^{\rm dis}$) of the events. The average of $P_{\rm dur}^{\rm dis}$ for each cluster is shown above the traces.

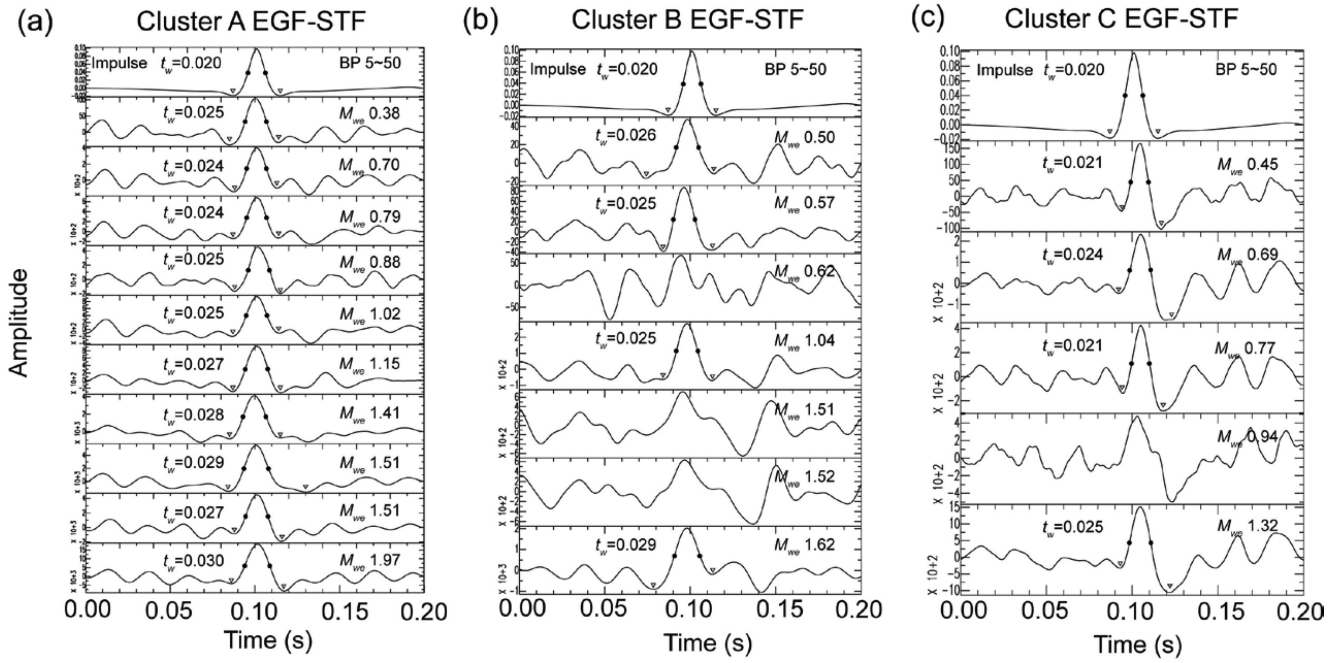

Figure 8. Source-time functions (STFs) determined using the empirical Green's function (EGF) method for (a) Cluster A, (b) Cluster B and (c) Cluster C. The magnitudes are indicated above each trace. The black dots indicate the half-pulse width of the STF of the events. The waveforms without dots are not used for pulse width determination because of a low signal-to-noise ratio.

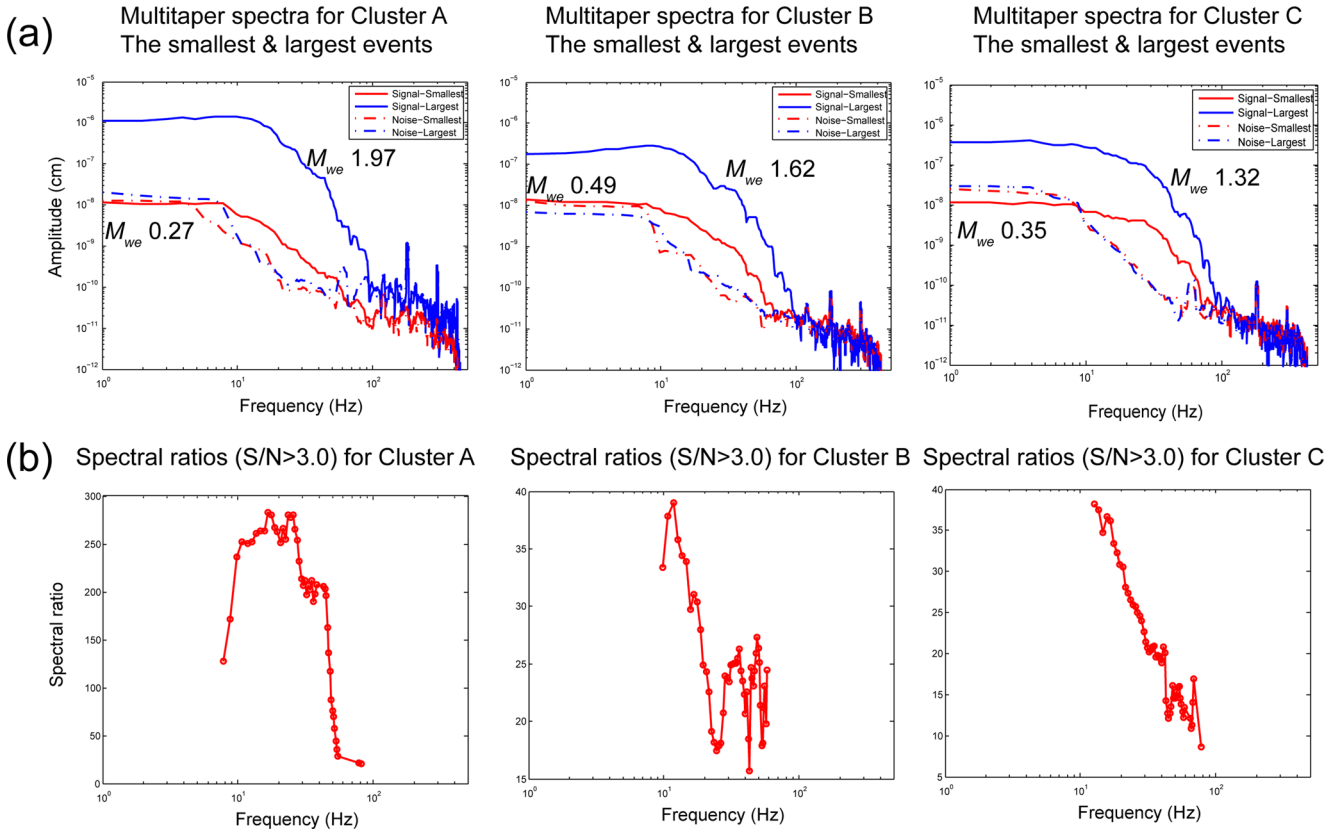

Figure 9. (a) Displacement spectra of the observed *Z*-component (*P* waves) for the smallest (red curve) and largest (blue curve) events in Clusters A (left), B (middle) and C (right). The multitaper spectral method (Thomson 1982) was used for calculating spectra. The red and blue dash-dot lines indicate the noise level of the smallest and largest events in the clusters, respectively. (b) Spectral ratios between the largest and smallest events for the three clusters. Appreciable drops in the ratio can be seen over the frequency band from 20 to 50 Hz for signal-to-noise ratios greater than 3.0.

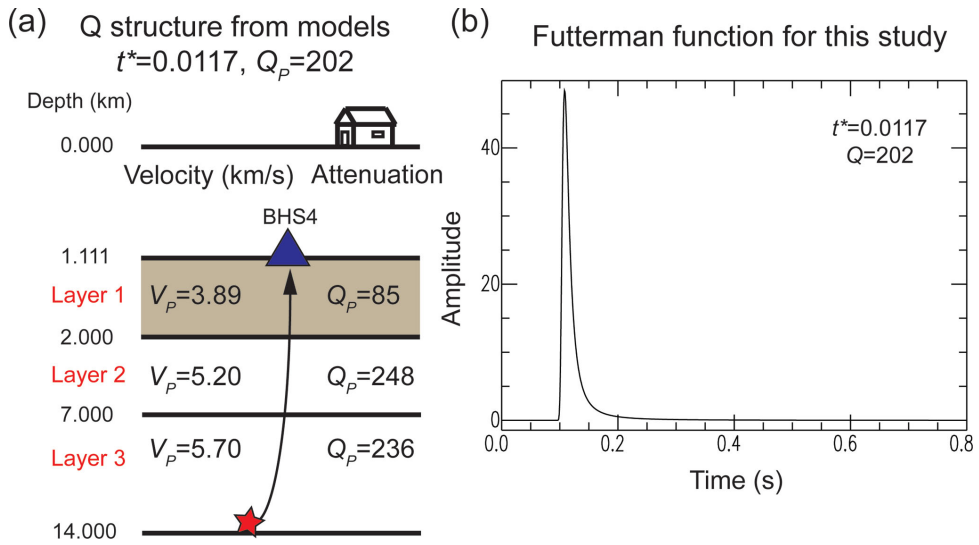

Figure 10. (a) Q-model ($Q_p = 202$, $t_P^* = 0.0117$) used in this study. (b) The Futterman function determined for the Q-structure shown in Fig. 10(a).

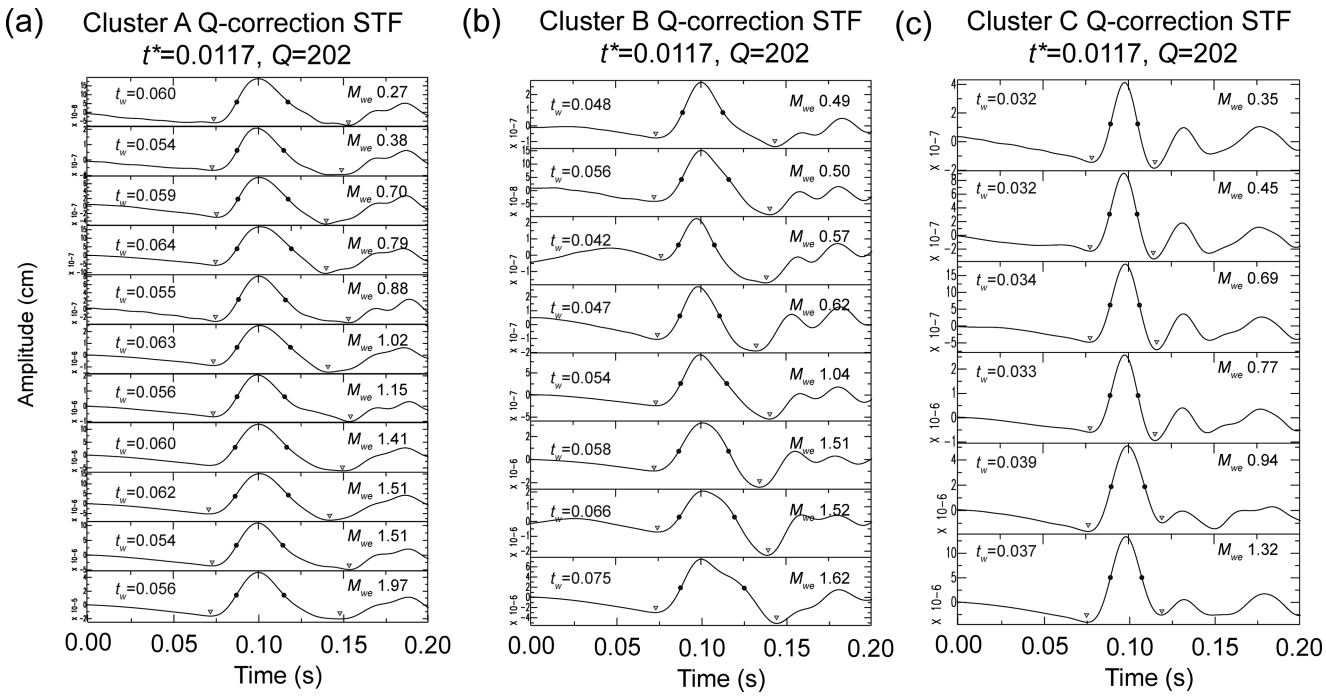

Figure 11. STFs determined using the Q-correction method and a zero-phase bandpass filter (5–50 Hz) for (a) Cluster A, (b) Cluster B and (c) Cluster C. The black dots and grey triangles on each trace indicate the half-pulse width and the left and right bottom amplitudes presented in Fig. 6.

moment-rate functions obtained by deconvolution are affected. In this case, the lower bound becomes somewhat uncertain. In particular, we cannot rule out the case in which the larger events have no broadening of their STFs and hence also appear impulsive, which would mean that all sources have durations below the data resolution of 0.02 s. However, such a case would require quite large and unusual attenuation, and hence it is unlikely, as shown in Section 6.

A plausible real situation is that the path effect is approximately accounted for by attenuation. Although we do not know the exact value of Q_p (Q for P waves) for the path involved, using the Q_p structure of the fault zone estimated from the data obtained by the TCDPBHS (Wang *et al*. 2012) and 3D Q tomography results for Taiwan (Wang *et al*. 2010), the average Q_p value estimated for the path from the source to the location of BHS4 (at a depth of approximately 1100 m) is approximately 202, which yields a t_P^* (P-wave traveltime divided by the path-averaged Q_p) of 0.0117s (Fig. 10a). Although this value may not strictly apply to our source station geometry, we use this value to estimate the width of the source pulse. The effect of attenuation on the waveform can be represented by a Futterman function (Futterman 1962), which is the impulse response of a dissipative medium. As shown in Fig. 10(b), the effective width of the Futterman function for $t_P^* = 0.0117$s is smaller than the width of the observed displacement pulses shown in Fig. 7. In this case, the difference between the width of the observed pulse and the effective width of the Futterman function is the approximate width of the source pulse, and we can estimate the width of the source pulses by deconvolving the observed waveforms with the Futterman function. As shown in Fig. 11(a), the source pulse width

is approximately 0.054 to 0.064 s (Table 1) and essentially constant. A smaller or larger t_P^* (i.e. a higher or lower Q_p, respectively) results in broader or narrower source pulses, respectively. Although we do not know the exact value of t_P^* for the path, the source pulse widths obtained are reasonable, as they are between those of the two end-member models.

5.1 Estimation of Q_p from *P*- and *S*-wave pulse width

Since the effect of attenuation is critical to our conclusion, we make an additional test to examine the effect of Q_P (t_P^*) by examining the pulse width difference between *P* and *S* waves. Since the observed *SH* waves are complex, probably because of the structure near the borehole, we assume that the first pulse of the *SH* wave on the *T*-component carries the path effect, and estimate t_P^* by comparing its pulse width to that of the *P* wave on the vertical component.

Assuming that the waveform change is solely due to attenuation, we can write

$$O_P(t) = S_P(t) * F(t; t_P^*), \tag{1}$$

$$O_S(t) = S_S(t) * F(t; t_S^*), \tag{2}$$

where $O_P(t)$, $S_P(t)$ and $F(t; t_P^*)$ are the observed waveform, the source time function and the Futterman function for the *P* wave, respectively. The corresponding functions for the *S* wave are given with a subscript 'S'. Using eqs (1) and (2), we can write the observed *S*-wave spectrum $\hat{O}_S(f)$ as

$$\hat{O}_S(f) = \hat{S}_S(f)\hat{F}(f; t_S^*) = \hat{O}_P(f)\left[\frac{\hat{S}_S(f)}{\hat{S}_P(f)}\right]\left[\frac{\hat{F}(f; t_S^*)}{\hat{F}(f; t_P^*)}\right], \tag{3}$$

where

$$\hat{F}(f; t_P^*) = \exp\left(-\pi f t_P^*\right) \exp\left(2if t_P^* \ln|f/f_H|\right), \tag{4}$$

$$\hat{F}(f; t_S^*) = \exp\left(-\pi f t_S^*\right) \exp\left(2if t_S^* \ln|f/f_H|\right), \tag{5}$$

which are derived from an absorption-band model (e.g. Kanamori & Anderson 1977; Kanamori & Rivera 2015). In eqs (4) and (5), f_H is the upper bound on the frequency of the absorption band and i is the imaginary unit. Although we do not know the exact value of f_H, as long as it is sufficiently higher than the frequency band we are concerned, it is not relevant to the waveform analysis.

First, we assume that the source spectrum is the same for the *P* and *S* waves except for a constant factor, that is, $[\frac{\hat{S}_S(f)}{\hat{S}_P(f)}] = c$ where c is a constant. Then, $[\frac{\hat{F}(f;t_S^*)}{\hat{F}(f;t_P^*)}]$ can be written as

$$\left[\frac{\hat{F}(f; t_S^*)}{\hat{F}(f; t_P^*)}\right] = \exp\left[-\pi f t_P^*(t_S^*/t_P^* - 1)\right] \times \exp\left[2if t_P^*(t_S^*/t_P^* - 1)\ln|f/f_H|\right]. \tag{6}$$

Relation (6) suggests that the form of $[\frac{\hat{F}(f;t_S^*)}{\hat{F}(f;t_P^*)}]$ is the same as that of $\hat{F}(f; t_P^*)$ in eq. (4), with t_P^* replaced by $t_P^*(t_S^*/t_P^* - 1)$. In our analysis, we use $t_s^*/t_p^* = 4$, $V_p/V_s = 1.73$ and $Q_p/Q_s = 2.25$ (Stein & Wysession 2003). Thus, eq. (3) leads to

$$O_S(t) = cO_P(t) * F(t; 3t_P^*). \tag{7}$$

We estimate t_P^* by the following procedure: compute $O_S(t)$ by convolving the observed *P*-wave pulse and the Futterman function with a given t_P^*, ranging from 0.010 to 0.030 s with 0.005 s interval, and compare the pulse width of the computed *S* pulse with that of the observed *SH* pulse. The comparison is illustrated in Fig. 12. The results indicate that reasonable values of t_P^* are 0.015–0.020, 0.020 and 0.010 for Clusters A, B and C, respectively, as shown in Fig. 12. The corresponding Q_p values are 112–150, 131 and 238 for Clusters A, B and C, respectively.

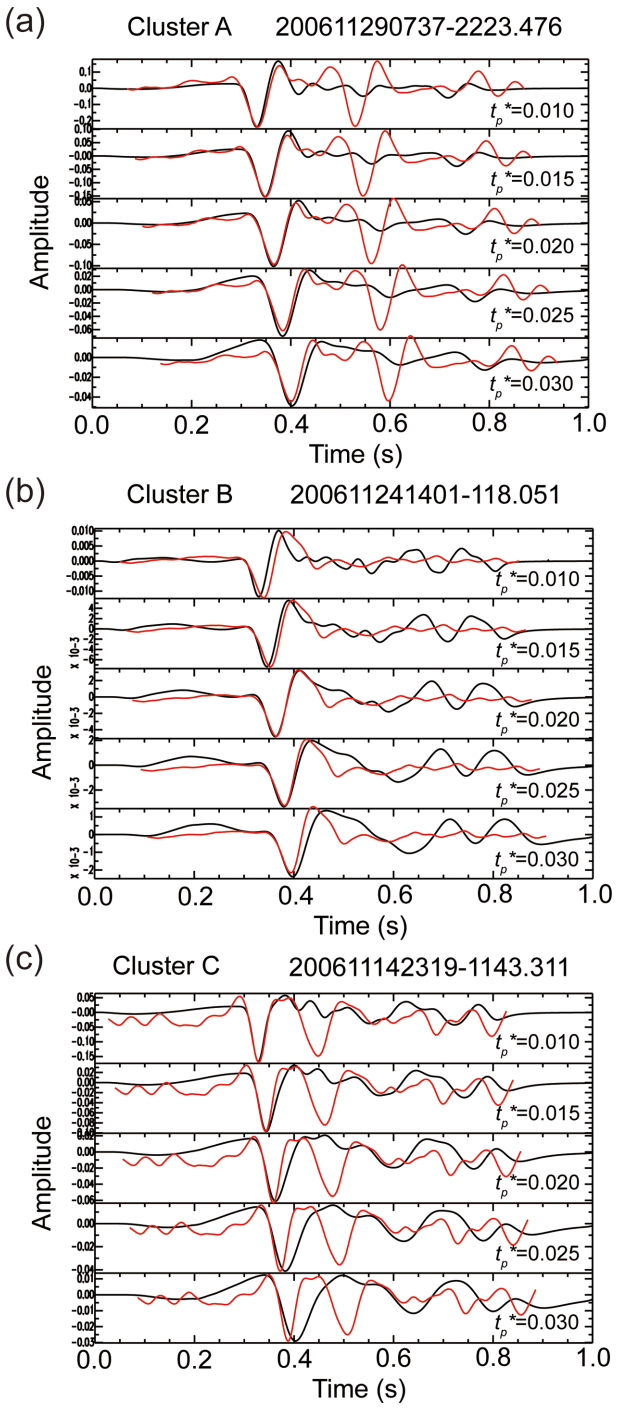

Figure 12. Comparison of the first pulse of the *SH* wave, $O_S(t)$, on the *T*-component (red lines) and $O_P(t) * F(t; 3t_P^*)$, convolution of the *P* wave on the vertical component and $F(t; 3t_P^*)$ with a given t_P^* (black lines), for (a) Cluster A, (b) Cluster B and (c) Cluster C.

In the above consideration, we assumed that $[\frac{\hat{S}_S(f)}{\hat{S}_P(f)}] = c$ which assumes that the corner frequency of the *P* wave, f_{cP}, is the same as that of the *S* wave, f_{cS}, but the observed ratio, f_{cP}/f_{cS} is commonly

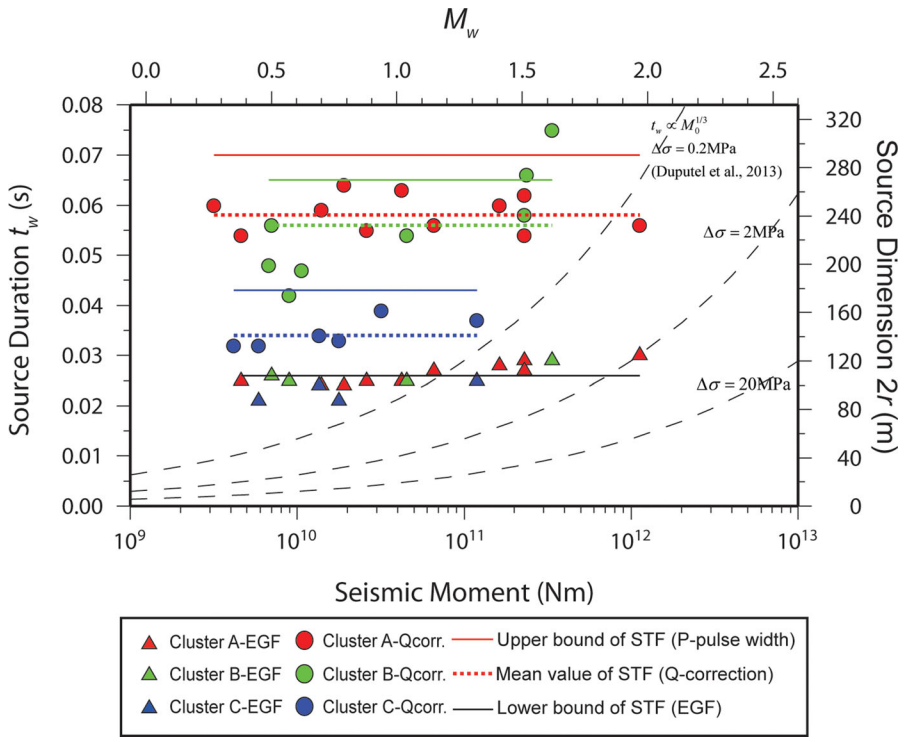

Figure 13. Source durations of events in Clusters A, B and C estimated using the three different methods. The red, green and blue symbols denote the results for Clusters A, B and C, respectively. The circles indicate the source durations (t_w) estimated using the Q-correction method. The dotted lines show the mean values for each cluster, and the triangles show the source durations (t_w) estimated using the EGF method, with the average indicated by a solid black line. The red, green and blue solid lines represent the upper bounds of the STF duration for Clusters A, B and C, respectively. The dashed black curves show the self-similarity relation ($t_w \propto M_0^{1/3}$) for constant stress drops of 0.2, 2, and 20 MPa. The curve labelled as $\Delta\sigma = 0.2$ MPa is close to that presented by Duputel *et al*. (2013). The right vertical axis gives the source dimension.

around 1.5, probably because of the finiteness of the source (e.g. Madariaga 1976). Then the *P*-wave source pulse should be shorter than *S*-wave pulse and the difference between the observed pulse widths of the *S* and *P* waves is partly due to the difference in corner frequency, and the effect of attenuation should be smaller than that estimated with the assumption $f_{cP} = f_{cS}$. Thus, t_P^* estimated above is the upper bound, and the actual t_P^* can be smaller, although the difference between them can be small.

6 DISCUSSION

6.1 Scaling of the STF

The source duration–seismic moment relations obtained using the three models, with different assumptions for path effects, consistently show that the source durations are essentially constant with respect to the seismic moment (Fig. 13), and hence they do not obey the self-similar empirical relation $t_w \propto M_0^{1/3}$ (e.g. Duputel *et al*. 2013) shown by dashed curves in Fig. 13. The mean values of the source duration estimated with the correction for Q (dotted lines) are 0.058, 0.056 and 0.034 s for Clusters A, B and C, respectively. Since these values are based on the attenuation values estimated for the region in prior studies, we use these values as representative solutions in this study. Notably, the scaling relation of Duputel *et al*. (2013), which was derived using large earthquakes over a magnitude range $M_w = 6.5$ to 9.2, yields a source duration of approximately 0.05 s, which is approximately equal to the source duration of the largest earthquake ($M_w = 1.97$) considered in the current study.

With the EGF method, the displacement record of the smallest event (i.e. the EGF) is thought to represent the upper bound of the path effect. Thus, deconvolution of the other events with the smallest event yields the smallest source moment-rate function within the resolution limits determined by the noise level (50 Hz). For example, as shown in Fig. 8(a), the pulse width of the largest event of Cluster A measured after applying the 5–50 Hz bandpass filter is 0.030 s. As shown in Fig. A2, this means that the source duration could be approximately 0.024 s without the filter, if the STF is triangular. The source durations for all other events are approximately the same, with the average being 0.017 s. Such lower bounds for the source duration imply that the stress drop (i.e. stress parameter) cannot be substantially higher than 2 MPa (Fig. 13).

Based on the EGF analysis alone, we cannot rule out that the source pulse is much narrower, since the obtained lower bounds of the pulse widths are on the boundary of the data resolution. Hence we cannot rule out the possibility of the commonly assumed scaling $t_w \propto M_0^{1/3}$ over a small range of t_w shorter than 0.02 s. However, such a case is unlikely as it would require much larger attenuation than determined in the region, as explained next.

Suppose that the sources have the scaling $t_w \propto M_0^{1/3}$, with a constant (and high) stress drop, for example, 20 MPa. Then, from the scaling relation shown in Fig. 13, t_w ranges from 0.002 to 0.012 s for M_w in the range of 0.3 to 2.0. For such sources, we compute the displacement P-pulses at our station for a suite of t_P^* from 0.010 to 0.045 s and measure the width of the displacement *P*-pulses thus computed, using the method illustrated in Fig. 6. Comparing the computed *P*-pulse widths for various t_P^* to the observed *P*-pulse widths shown in Fig. 7, we find that t_P^* of 0.035, 0.030

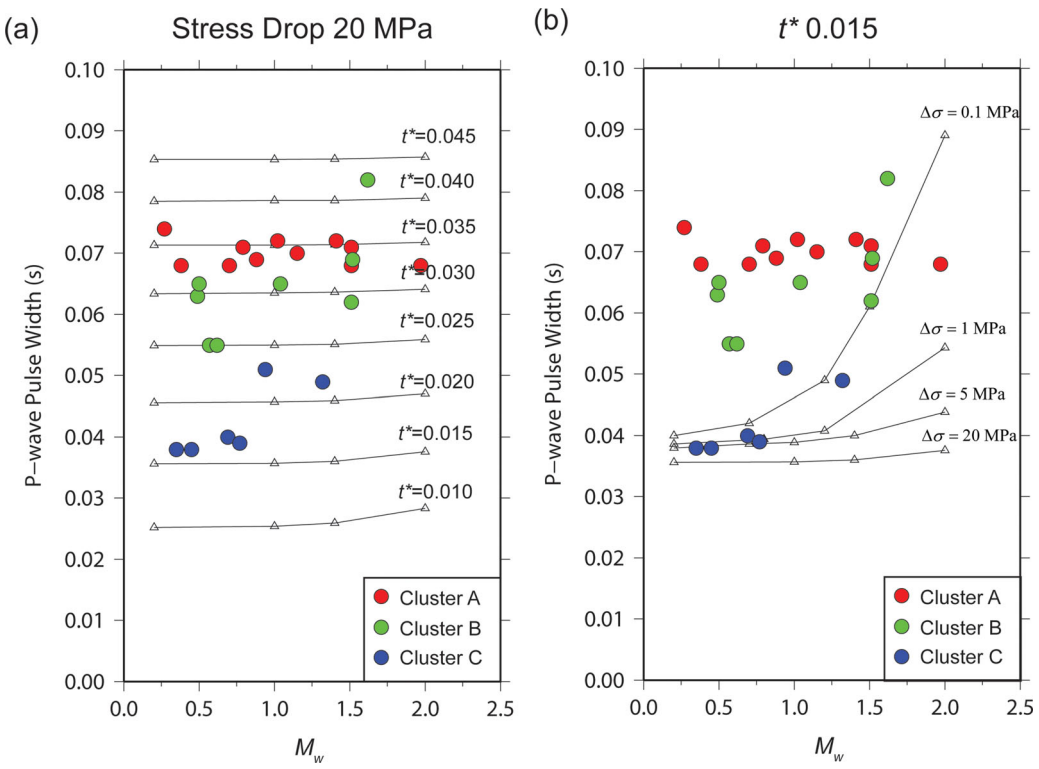

Figure 14. (a) Comparison between the computed *P*-pulse widths of an event with a stress drop of 20 MPa and observations. The triangles and lines represent the computed *P*-pulse widths for a suite of t_P^* from 0.010 to 0.045 s. Red, green and blue circles indicate the observed pulse widths of the *P* waves for Clusters A, B and C, respectively. (b) Comparison between the computed *P*-pulse widths of an event with a t_P^* of 0.015 and observations. The triangles and lines represent the computed *P*-pulse widths for a suite of stress drop from 0.1 to 20 MPa.

and 0.015 s is required to match the observations for Clusters A, B and C, respectively (Fig. 14a). These values of t_P^* are too large compared both with the value inferred from Wang *et al*. (2010) and Wang *et al*. (2012) ($t_P^* = 0.0117$ s) and with the upper bounds estimated in Section 5 from the pulse-width difference between *P* and *S* waves ($t_P^* = 0.015$–0.020, 0.020, 0.010 s for Clusters A, B and C, respectively), even if we allow for the possibility of uncertainties in the t_P^* measurements. The discrepancy is especially substantial for Clusters A and B. The results for Cluster C can be reconciled with the constant-stress-drop scaling for $t_P^* = 0.015$ s, which is too large but perhaps still realistic. However, even this higher-than-observed value of $t_P^* = 0.015$ s is insufficient to explain the results for Clusters A and B, for any value of (constant) stress drop, as illustrated in Fig. 14(b).

We also compare the *P*-wave pulse width $P_{\rm dur}^{\rm vel}$ between the events within the clusters and the nearby areas within less than 2 km. As shown in Fig. 15, some of these nearby events have shorter $P_{\rm dur}^{\rm vel}$ compared with the events within the clusters. Since these events should experience similar attenuation and path effects in general, their shorter $P_{\rm dur}^{\rm vel}$ suggests that the *P*-wave pulse width indeed contains information about the source, and it is not merely dominated by the attenuation.

6.2 Potential physical explanations for the constant duration

What can cause the observed constant source duration? There can be several explanations, the plausibility of which needs to be further studied, for example, using numerical models.

One possibility is that all events in each cluster rupture the same seismogenic patch of a certain size. We can interpret our duration results in terms of the source dimension of an assumed circular fault with rupture velocity $V_{\rm rup} = 0.75V_s$ where V_s is the shear-wave velocity. This assumption is commonly used in estimating the source dimension from spectral corner frequency (Brune 1970). We assume that all events in this study occurred on the same fault plane (350, 35, −140), which is shown in Fig. 1(c). Then, the angle between the normal to the fault plane and the outgoing ray is given by $\theta = 152^\circ$; $V_{\rm rup}$ is 2505 m s^{-1} and the *P*-wave velocity in the source region is given by $V_p = 5700$ m s^{-1}. Thus, the dimension $2r$ can be estimated from the relation presented by Lanza *et al*. (1999):

$$r = \frac{t_w V_{\rm rup}}{1 + V_{\rm rup} \sin\theta / V_p}, \tag{8}$$

and the range of rupture lengths $2r$ of the events in Clusters A, B and C are 100–260 m, 100–310 m and 80–160 m, respectively (Table 1). For the specific model where we assume a *Q*-structure (i.e. *Q*-correction method), the source dimensions are 242, 232 and 144 m, respectively.

In this model, all events in each cluster, regardless of the magnitude, are hosted on a patch of the corresponding size, with events of different magnitude corresponding to different stress drops, for example, ranging from 0.0007 to 0.32 MPa in Cluster A. The difference in stress drops can be caused by time-dependent variations in pre-stress and other patch properties, for example, due to variations in pore pressure; during rupture propagation, such differences could be strongly coupled to differences in the rupture mode, amount of slip and amount of co-seismic (dynamic) weakening. Numerical studies can help identify plausible situations that can lead to the implied variations in stress drop over the same seismogenic patch. The assumption that all events for each cluster are contained within the same seismogenic patch suggests that the patch is surrounded

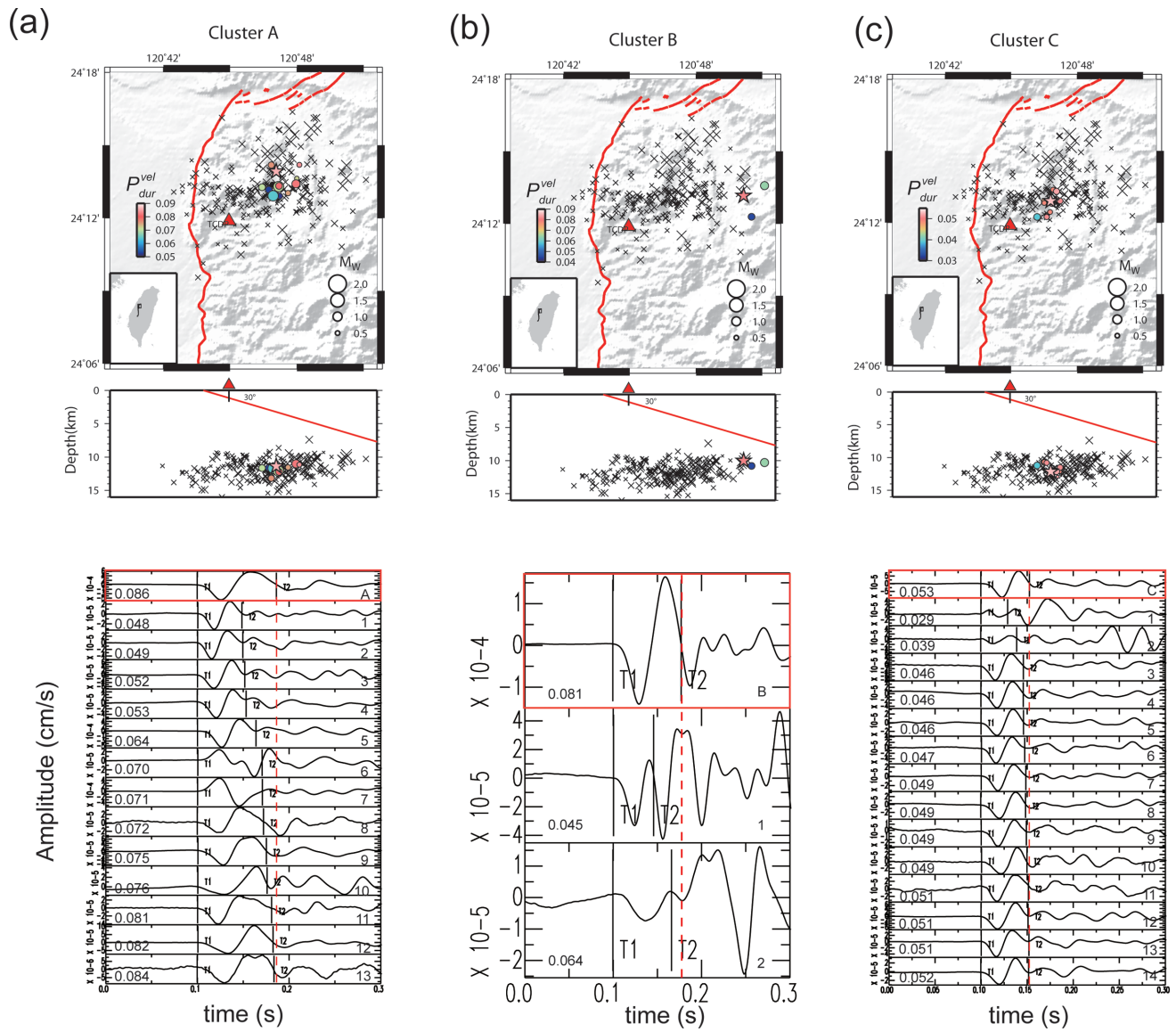

Figure 15. Events near the cluster with a shorter duration P_{dur}^{vel} compared to an event in (a) Cluster A, (b) Cluster B and (c) Cluster C. Locations of the nearby events (circles) and the cluster (asterisk) are shown in the upper section. The colour and size of the circles indicate the duration P_{dur}^{vel} and magnitude of the events, respectively. The crosses are the events in the background. The *Z*-component velocity waveforms for the event inside the cluster (top trace in the red box) and the nearby events are shown in the lower section. The duration P_{dur}^{vel} is measured between T1 and T2 markers. The red dashed line is drawn at the T2 marker of the cluster event as a reference. The estimated P_{dur}^{vel} is indicated on each trace.

by aseismic fault regions capable of containing seismic slip, at least for such small events; this can be accomplished by sufficient rate-strengthening properties of the fault outside the patch. Since the source dimensions here are estimated using a dynamic rupture speed, this implies that the corresponding source size is due to dynamic rupture propagation, and hence may be unrelated to the nucleation which is a quasi-static process; in particular, the nucleation size can be much smaller than the estimated source dimensions.

Alternatively, the constant duration may be related to the nucleation size. The identified clusters contain some of the smallest earthquakes observed in the region, implying that at least those smallest events may be controlled by the nucleation processes, perhaps arresting right after nucleation due to unfavourable conditions outside the nucleation patch. Since the duration of all events is the same, one can hypothesize that all events in each cluster are controlled by the nucleation. In this model, estimating the source dimension using the traditional assumption on constant rupture speeds may not be relevant, since rupture speeds right after nucleation and right before arrest are likely to be much smaller than the (average) estimates of 0.75 *Vs*. It remains to be seen whether a physical model can be created in which the nucleation size remains constant—implying a constancy in a number of fault properties, including the effective normal stress—while events spontaneously arrest shortly after nucleation, with significant variations in their stress drop.

Another possibility is that the identified seismic events are caused and driven by rapid external factors, for example, bursts of fluid into the fault zone due to episodic hydrofracturing. In that case, the duration is controlled by the physics of the external factor. Pore pressure variations due to fluid injection into the fault zone from the surrounding rocks have been hypothesized to play a significant role in triggering episodic slow slip in subduction zones (Liu & Rice 2005, 2007). In those models, the fluid injection and pore pressure

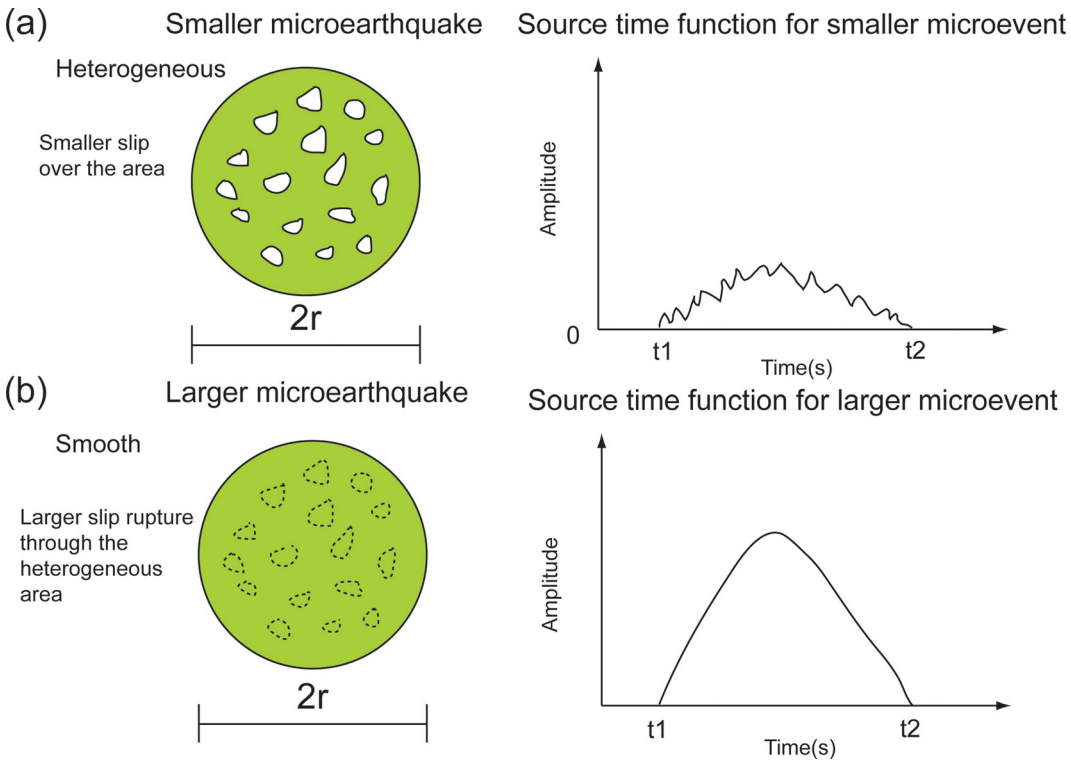

Figure 16. Schematic of (a) small and (b) large earthquakes, motivated by the spectral ratios shown in Fig. 9. The white irregular circles represent stronger asperities that delay or stop rupture for small events, exciting high-frequency energy (illustrated in the right column). Schematic of slip distributions are shown on the left, and the associated STFs are shown on the right.

variation is a quasi-static process, but perhaps such processes can be dynamic on the small temporal and spatial scales corresponding to the observed events.

The study of Lengliné *et al*. (2014) showed that microearthquakes during a water circulation test in a geothermal reservoir had very similar properties to the events studied here. In particular, the study identified clusters of microearthquakes with constant duration but substantially different magnitudes, similar to our Clusters A–C, and hypothesized that the large differences in magnitudes, linked by Lengliné *et al*. (2014) to differences in slip and hence stress drop, are due to pore pressure effects. Their discussion focused on aseismic pore pressure processes, in which fluids trigger aseismic fault slip which, in turn, triggers microearthquakes on asperities. The injection-induced variations of pore pressure may indeed cause or contribute to the inferred variations in stress drops. However, by itself, the model with fluid-induced aseismic slip may not explain the constancy of the event durations; for that, an additional assumption of isolated seismogenic patches seems to be needed, as already discussed. An alternative fluid-related possibility is that the slip is driven by a rapid local fluid injection into the fault zone. The associated rapid increase in pore pressure would cause a rapid drop in fault strength and induce rapid (seismic) slip. Once the local fluid injection episode is exhausted (or significantly slows), the slip would cease to be seismic, provided that the scale of the process is below the local nucleation size or the fault has stable (e.g. velocity-strengthening) friction properties. In this mechanism, the duration is controlled not by the fault properties but rather the fluid movements.

6.3 Variation of spectral shape at high frequency

Although the smallest and largest events within each cluster have approximately the same duration, their spectral shapes are different at very high frequencies, above 20 Hz. Fig. 9(a) shows the multitaper displacement spectra (Thomson 1982) of *Z*-component *P* waves for the smallest and largest events in Clusters A, B and C. The noise levels for the smallest and largest events in each cluster are also shown. Fig. 9(b) shows the spectral ratio of the largest event to the smallest one. The spectral ratio shows an appreciable drop in the frequency band 20–50 Hz for all clusters, indicating that the smallest earthquake is relatively richer in high-frequency energy compared with the largest earthquake. Since these events are within the same cluster, they should have the same path effect (attenuation), and we can attribute the different frequency content to the source effects.

Differences in the spectral shape between the largest and smallest earthquakes at high frequencies for each cluster should be investigated, for example, through numerical modelling of the earthquake source. One hypothesis is that the difference can result from heterogeneity or roughness of the source patch, as schematically illustrated in Fig. 16. When rupture is stopped or delayed at a strong asperity within the source patch (illustrated by the irregular circles in Fig. 16), the high-frequency radiation is enhanced (e.g. Lapusta & Liu 2009). Smaller events would correspond to a smaller slip for the same source size and hence may be incapable of rupturing stronger asperities, as illustrated in Fig. 16(a); this produces multiple arrest fronts that radiate high frequencies. In contrast, larger events potentially rupture some or all such asperities, resulting in smoother rupture and hence less high-frequency content. This hypothetical model is consistent with smaller stress drops for smaller events and the constant source duration. The constant duration would be the result of the same overall source size. The smaller stress drops for smaller events would be the result of smaller slip over the patch. When the rupture cannot break the stronger asperities, the slip next to the asperities is suppressed, and the average slip per seismogenic patch (the circle in Fig. 16) would be smaller. Since the stress drop

scales with the ratio of slip to the patch size, smaller average slip implies smaller stress drop. Every time slip goes around an asperity, its shear stress increases due to the slip mismatch, bringing the stress on the asperity closer to its (higher) strength. Even though such a scenario creates heterogeneous stress on the fault before a larger event, the patch also has heterogeneous strength, so that mismatch between stress and strength is actually decreased, potentially creating smoother slip during larger events and hence not as much high-frequency seismic signals.

7 CONCLUSIONS

Using high-quality seismic data from a vertical borehole array installed in central Taiwan, we identified several seismic clusters with high waveform similarity and magnitudes ranging from 0.3 to 2.0. To investigate the source scaling, we removed the path effect by using an EGF method and a path-averaged Q-correction method. In both analyses, the results indicate a nearly constant source duration for events with $M_w \leq 2.0$ within the clusters, violating the commonly used scaling relation $t_w \propto M_0^{1/3}$. If we assume a constant rupture speed within each cluster, this constant duration corresponds to a characteristic length, which may correspond to the size of an isolated seismogenic patch that hosts the cluster events. In this model, events of different slip and hence stress drop would be created by heterogeneity within the patch. The constant duration may also be related to the nucleation processes or outside triggering factors. Further observational and numerical studies are needed to test and distinguish between these potential explanations.

ACKNOWLEDGEMENTS

We thank Dr Volker Oye at NORSAR, Norway, providing the Microseismic Monitoring (MIMO) for our seismic clusters location. We appreciate the helpful comments from the Associated Editor, two referees and Prof Luis Rivera, who helped us to improve this manuscript. Support from the Graduate Students Study Abroad Program 101-2917-I-008-001- of the National Science Council (NSC) contributed to this international collaboration. This research was supported by the Taiwan Earthquake Research Center (TEC) funded through the Ministry of Science and Technology (MoST) with grant number 104-2116-M-008-011. The TEC contribution number for this paper is 00119.

REFERENCES

Abercrombie, R.E., 1995. Earthquake source scaling relationships from –1 to 5 M_L using seismograms recorded at 2.5-km depth, *J. geophys. Res.,* **100**(12), 24 015–24 036.

Aki, K., 1967. Scaling law of seismic spectrum, *J. geophys. Res.,* **72**(4), 1217–1231.

Allmann, B.P. & Shearer, P.M., 2009. Global variations of stress drop for moderate to large earthquakes, *J. geophys. Res.,* **114,** B01310, doi:10.1029/2008JB005821.

Bouchon, M., Karabulut, H., Aktar, M., Ozalaybey, S., Schmittbuhl, J. & Bouin, M., 2011. Extended nucleation of the 1999 M_w 7.6 Izmit earthquake, *Science,* **331,** 877–880.

Brune, J., 1970. Tectonic stress and the spectra of seismic shear waves from earthquakes, *J. geophys. Res.,* **75**(26), 4997–5009.

Duputel, Z., Tsai, V., Rivera, L. & Kanamori, H., 2013. Using centroid time-delays to characterize source durations and identify earthquakes with unique characteristics, *Earth Planet Sci. Lett.,* **375,** 92–100.

Futterman, W., 1962. Dispersive body waves, *J. geophys. Res.,* **67**(13), 5279–5291.

Harrington, R. & Brodsky, E., 2009. Source duration scales with magnitude differently for earthquakes on the San Andreas fault and on secondary faults in Parkfield, California, *Bull. seism. Soc. Am.,* **99,** 2323–2334.

Ide, S., Beroza, G.C., Prejean, S.G. & Ellsworth, W.L., 2003. Apparent break in earthquake scaling due to path and site effects on deep borehole recordings, *J. geophys. Res.,* **108**(5), 2271–2284.

Ide, S., Matsubara, M. & Obara, K., 2004. Exploitation of high-sampling Hi-net data to study seismic energy scaling: the aftershocks of the 2000 western Tottori, Japan, earthquake, *Earth Planets Space,* **56,** 859–871.

Kanamori, H. & Anderson, D., 1977. Importance of Physical dispersion in surface wave and free oscillation problems: review, *Rev. Geophys. Space Phys.,* **15**(1), 105–112.

Kanamori, H. & Rivera, L., 2015. Near-vertical multiple ScS phases and vertically averaged mantle properties, in *The Interdisciplinary Earth: A Volume in Honor of Don L. Anderson,* vol. 71, pp. 9–31, eds Foulger, G.R., Lustrino, M. & King, S.D., Geological Society of America Special Paper 514 and American Geophysical Union Special Publication.

Kim, K., Chiu, J., Pujol, J., Chen, K., Huang, B., Yeh, Y. & Shen, P., 2005. Three-dimensional V_P and V_S structural models associated with the active subduction and collision tectonics in the Taiwan region, *Geophys. J. Int.,* **162,** 204–220.

Lanza, V., Spallarossa, D., Cattaneo, M., Bindi, D. & Augliera, P., 1999. Source parameters of small events using constrained deconvolution with empirical Green's functions, *Geophys. J. Int.,* **137,** 651–662.

Lapusta, N. & Liu, Y., 2009. Three-dimensional boundary integral modeling of spontaneous earthquake sequences and aseismic slip, *J. geophys. Res.,* **114,** B09303, doi:10.1029/2008JB005934.

Lengliné, O., Lamourette, L., Vivin, L., Cuenot, N. & Schmittbuhl, J., 2014. Fluid-induced earthquakes with variable stress drop, *J. geophys. Res.,* **119,** 8900–8913.

Lin, Y.Y., 2014. TCDP borehole seismometers array – microearthquake observations and seismic source characteristics investigation, *PhD thesis,* National Central University, Zhongli, Taiwan (in Chinese).

Lin, Y.Y., Ma, K.F. & Oye, V., 2012. Observation and scaling of microearthquakes from the Taiwan Chelungpu-fault borehole seismometers, *Geophys. J. Int.,* **190,** 665–676.

Liu, Y. & Rice, J.R., 2005. Aseismic slip transients emerge spontaneously in 3D rate and state modeling of subduction earthquake sequences, *J. geophys. Res.,* **110,** B08307, doi:10.1029/2004JB003424.

Liu, Y. & Rice, J.R., 2007. Spontaneous and triggered aseismic deformation transients in a subduction fault model, *J. geophys. Res.,* **112,** B09404, doi:10.1029/2007JB004930.

Ma, K.F. *et al.*, 2006. Slip zone and energetics of a large earthquake from the Taiwan Chelungpu-fault Drilling Project, *Nature,* **444,** 473–476.

Ma, K.F., Lin, Y.Y., Lee, S.J., Mori, J. & Brodsky, E.E., 2012. Isotropic events observed with a borehole array in the Chelungpu fault zone, Taiwan, *Science,* **337,** 459–463.

Madariaga, R., 1976. Dynamics of an expanding circular fault, *Bull. seism. Soc. Am.,* **66,** 639–666.

Mayeda, K. & Malagnini, L., 2009. Apparent stress and corner frequency variations in the 1999 Taiwan (Chi-Chi) sequence: evidence for a step-wise increase at $M_w \sim 5.5$, *Geophys. Res. Lett.,* **36,** L10308, doi:10.1029/2009GL037421.

Mori, J., Abercrombie, R. & Kanamori, H., 2003. Stress drops and radiated energies of aftershocks of the 1994 Northrigde, California, earthquake, *J. geophys. Res.,* **108**(11), 2545–2557.

Oye, V. & Roth, M., 2003. Automated seismic event location for hydrocarbon reservoirs, *Comput. Geosci.,* **29,** 851–863.

Oye, V., Bungum, H. & Roth, M., 2005. Source parameters and scaling relations for mining-related seismicity within the Pyhasalmi Ore Mine, Finland, *Bull. seism. Soc. Am.,* **95**(3), 1011–1026.

Reasenberg, P.A. & Oppenheimer, D., 1985. FPFIT, FPPLOT, and FPPAGE: fortran computer programs for calculating and displaying earthquake fault-plane solutions, U.S. Geol. Surv. Open-File Rep., 85–739.

Rice, J., 1993. Spatio-temporal complexity of slip on a fault, *J. geophys. Res.,* **98,** 9885–9907.

Rice, J. & Ruina, A., 1983. Stability of steady frictional slipping, *J. Appl. Mech.,* **50,** 343–349.

Rubin, A. & Ampuero, J., 2005. Earthquake nucleation on (aging) rate and state faults, *J. geophys. Res.,* **110**(B1), B11312, doi:10.1029/2005JB003686.

Stein, S. & Wysession, M., 2003. *An Introduction to Seismology, Earthquakes, and Earth Structure,* Blackwell Publishing Ltd, 192 pp.

Stork, A.L. & Ito, H., 2004. Source parameter scaling for small earthquakes observed at the Western Nagano 800-m-deep borehole, Central Japan, *Bull. seism. Soc. Am.,* **94**(5), 1781–1794.

Thomson, D.J., 1982. Spectrum estimation and harmonic analysis, *Proc. IEEE,* **70,** 1055–1096.

Venkataraman, A., Beroza, G.C., Ide, S., Imanishi, K., Ito, H. & Iio, Y., 2006. Measurements of spectral similarity for microearthquakes in western Nagano, Japan, *J. geophys. Res.,* **111,** B03303, doi:10.1029/2005JB003834.

Wang, Y.J., Ma, K.F., Mouthereau, F. & Eberhart-Phillips, D., 2010. Three dimensional Q_p- and Q_s-tomography beneath Taiwan Orogenic Belt: comparison to the tectonic and the thermal structure, *Geophys. J. Int.,* **180,** 891–910.

Wang, Y.J., Lin, Y.Y., Ma, K.F. & Lee, M.C., 2012. Fault zone Q values derived from Taiwan Chelungpu Fault borehole seismometers (TCDPBHS), *Tectonophysics,* **578,** 76–86.

Yamada, T., Mori, J., Ide, S., Abercrombie, R.E., Kawakata, H., Nakatani, M., Iio, Y. & Ogasawara, H., 2007. Stress drops and radiated seismic energies of microearthquakes in a South African gold mine, *J. geophys. Res.,* **112,** B03305, doi:10.1029/2006JB004553.

APPENDIX A: RECORDS AT THE SEVEN TCDPBHS STATIONS, BHS1–BHS7, OF THE LARGEST EVENT

Fig. A1 shows the records at the seven TCDPBHS stations, BHS1–BHS7, of the unfiltered Z-component (P wave) velocity seismograms of the largest event. The records are similar for all the stations, as expected given the distance of 10–15 km to the sources and the spatial extent of the array of ∼300 m.

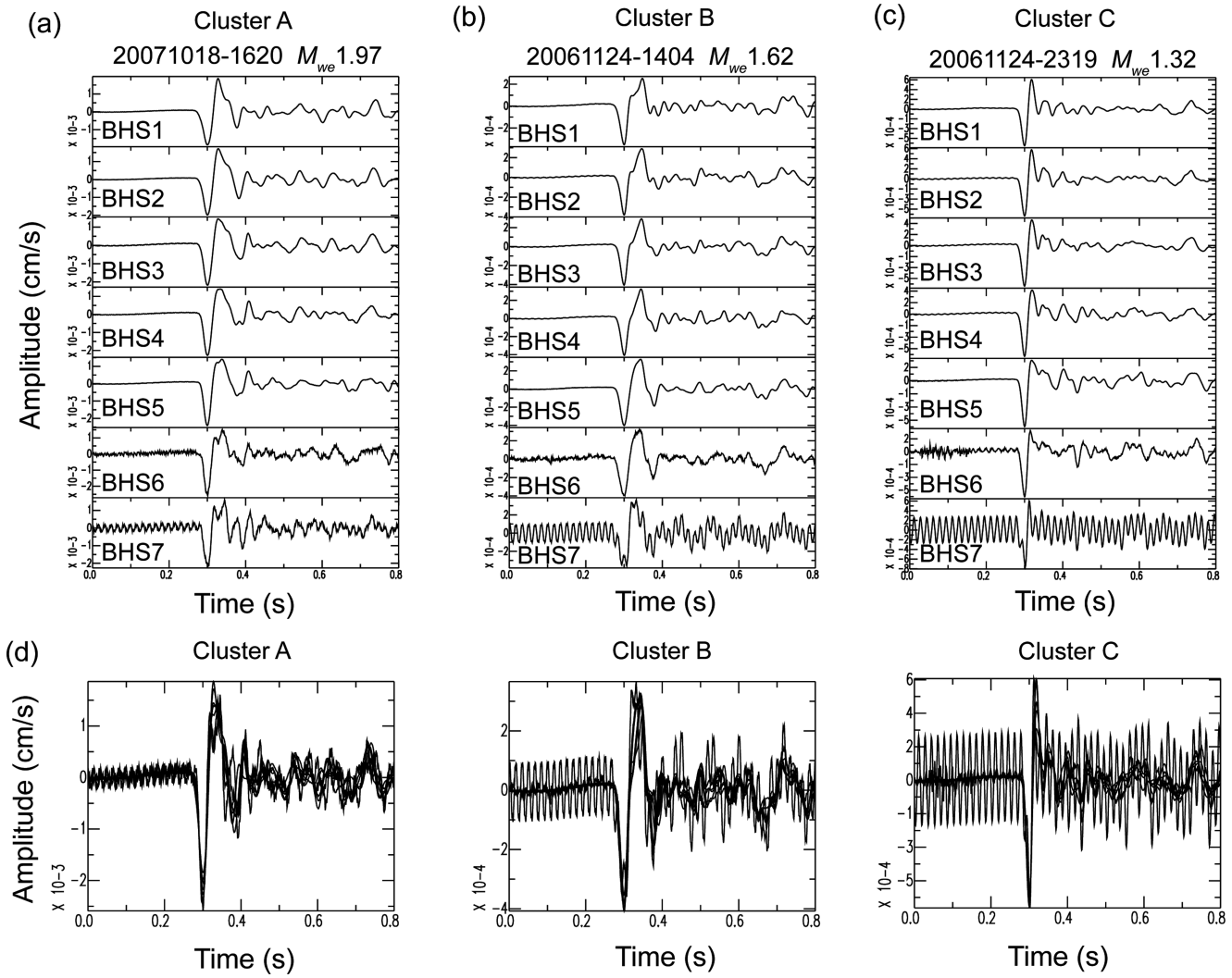

Figure A1. Records at the seven TCDPBHS stations, BHS1–BHS7, of the unfiltered Z-component (P wave) velocity seismograms of the largest event of (a) Cluster A, (b) Cluster B and (c) Cluster C. The records are similar for all the stations, as expected given the distance of 10–15 km to the sources and the spatial extent of the array of ∼300 m. (d) Comparison of the P-wave records for Clusters A (left), B (middle) and C (right).

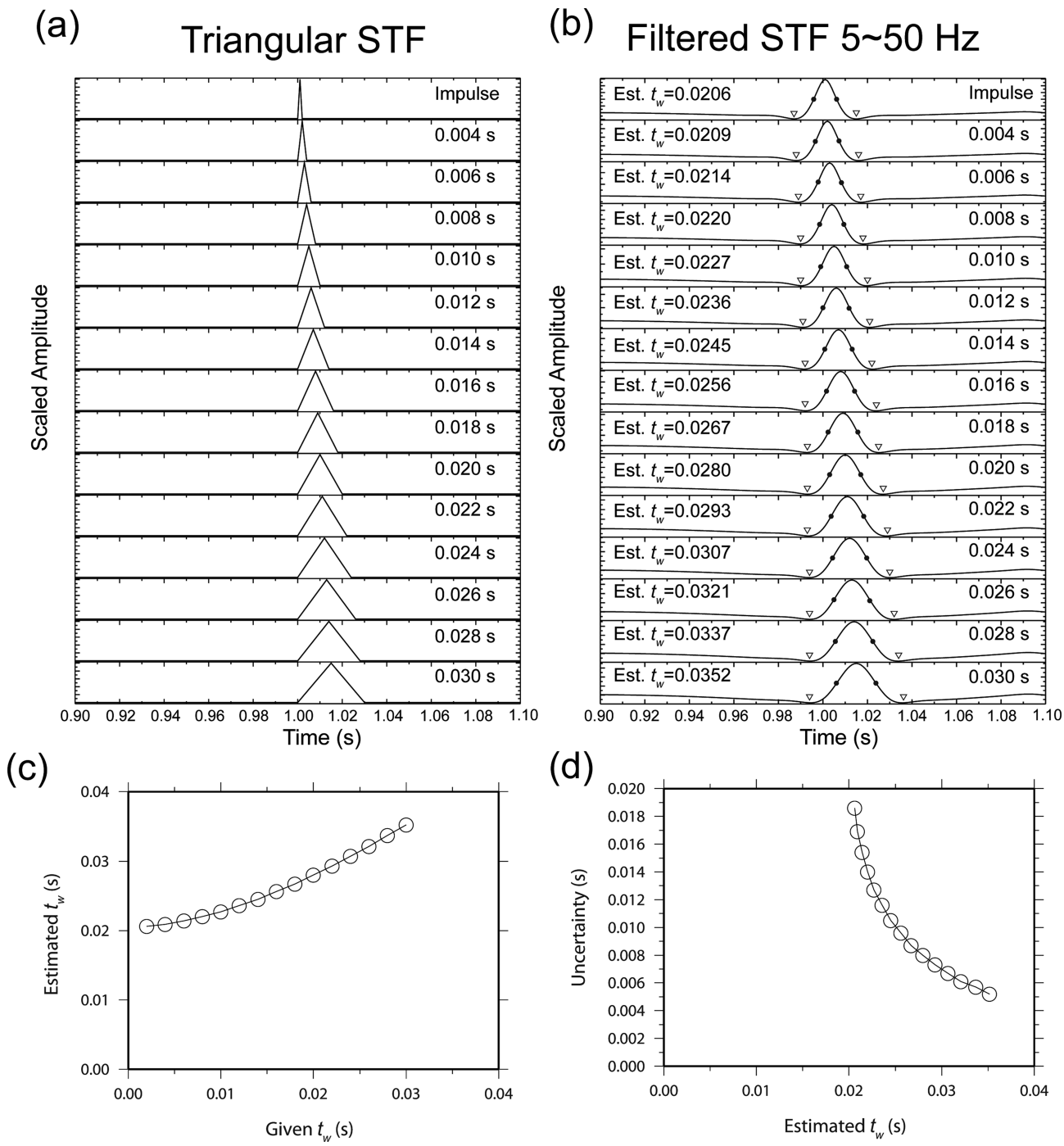

Figure A2. Effect of the bandpass filter on the pulse width measurement of the STF. (a) Triangular STF with t_w ranging from 0.002 to 0.030 s. (b) Waveforms filtered by a zero-phase bandpass filter with a passband of 5–50 Hz. The pulse widths are measured using the method illustrated in Fig. 6 and indicated on the left of the waveforms. (c) Comparison of the given t_w and estimated t_w. (d) The difference between the estimated and the given t_w as a function of the estimated t_w.

APPENDIX B: EFFECT OF BANDPASS FILTER ON PULSE WIDTH MEASUREMENTS

Fig. A2(a) shows a series of triangular pulses representing STFs. Fig. A2(b) shows the waveforms after we applied a zero-phase bandpass filter with a passband of 5–50 Hz to the STFs in Fig. A2(a). When the pulse width is small, the broadening is appreciable, but as the pulse width increases, broadening becomes relatively insignificant. Fig. A2(c) shows the relation between the given pulse width t_w (Fig. A2a) and the pulse width of the filtered waveforms (Fig. A2b) estimated using the method described in the text. Fig. A2(d) shows the difference between the estimated and given pulse widths.